Journal Pre-proof

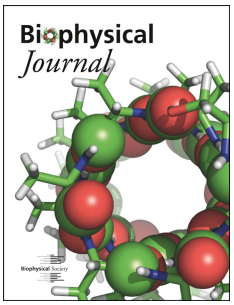

An energy-based mathematical model of actin-driven protrusions in eukaryotic chemotaxis

Samuel W.S. Johnson, Maddy Parsons, Ruth E. Baker, Philip K. Maini

PII: S0006-3495(26)00543-6

DOI: https://doi.org/10.1016/j.bpj.2026.08.001

Reference: BPJ 14472

To appear in: *Biophysical Journal*

Received Date: 6 October 2025

Accepted Date: 3 August 2026

Please cite this article as: Johnson SWS, Parsons M, Baker RE, Maini PK, An energy-based mathematical model of actin-driven protrusions in eukaryotic chemotaxis, *Biophysical Journal* (2026), doi: https://doi.org/10.1016/j.bpj.2026.08.001.

Manuscript submitted to **Biophysical***Journal*
Article

An energy-based mathematical model of actin-driven protrusions in eukaryotic chemotaxis

Samuel W.S. Johnson[1,*], Maddy Parsons[2], Ruth E. Baker[1], and Philip K. Maini[1]

[1]Wolfson Centre for Mathematical Biology, Mathematical Institute, University of Oxford, Oxford, United Kingdom
[2]Randall Centre for Cell and Molecular Biophysics, King's College London, London, United Kingdom
[*]Correspondence: samuel.johnson@maths.ox.ac.uk

ABSTRACT In eukaryotic cell chemotaxis, many cells extend and retract transient actin-driven protrusions at their membrane that facilitate both the detection of external chemical gradients and directional movement via cell–matrix coupling and traction. Although extensive experimental work has detailed how cellular protrusions and morphology vary under different environmental conditions, the mechanistic principles linking protrusive activity to these factors remain poorly understood. Here, we model the extension of actin-based protrusions in chemotaxis as an optimisation problem, wherein cells balance the detection of chemical gradients with the energetic cost of protrusion formation. Our model, built on the assumption of maximal energetic efficiency during migration, provides a framework that qualitatively reproduces experimentally observed patterns of protrusive activity across a range of biological systems and environmental conditions, suggesting that energetic efficiency may underpin the morphology and chemotactic behaviour of motile eukaryotic cells. Additionally, we leverage the model to generate novel predictions regarding cellular responses to other, experimentally untested environmental perturbations, providing testable hypotheses for future experimental work that may be used to validate and refine the model presented here.

SIGNIFICANCE This work provides a phenomenological optimisation framework for understanding how eukaryotic cells regulate actin-driven protrusions during chemotaxis. By casting protrusion formation as an energy optimisation problem in which the accuracy of gradient detection is balanced with energy expenditure, the model bridges cell morphology, environmental sensing, and energetic constraints. The insights generated by this model advance the theoretical basis of eukaryotic cell chemotaxis and highlight energy optimisation as a potential unifying principle of cell behaviour. The framework is qualitatively consistent with existing trends reported in the experimental literature and generates testable hypotheses for future experiments, enabling deeper investigation of how cells integrate physical and chemical cues to guide migration.

1 INTRODUCTION

Chemotaxis is the directed migration of cells in response to chemical gradients and it underpins many biological processes, from the immune response to embryonic development (1, 2). In cancer, the ability of malignant cells to detect and traverse gradients of growth factors and chemokines drives their invasion into surrounding tissues (3). In many of these processes, cells extend and retract transient actin-based protrusions at their membrane to sample external chemical gradients and to generate locomotive forces for migration (4). However, despite their importance in chemotaxis, the regulatory mechanisms that govern protrusive dynamics in motile eukaryotic cells remain incompletely understood. Experimental studies have provided detailed insight into how environmental parameters shape cell morphology and motility (5–7). However, because such studies are necessarily focused on specific perturbations and systems, it remains challenging to extract general mechanistic principles linking cell behaviours to environmental constraints. While it is known that cells modulate their protrusive activity in response to multiple environmental factors, including the mechanical properties of the substrate (5, 8–10) and the properties of the chemical gradient along which they migrate (11, 12), it is not clear mechanistically how these factors drive such morphological changes. A better understanding of how various environmental factors regulate the protrusive activity of cells would offer insights into how cell motility may be controlled *in vivo*, and hence how, for example, immune responses can be expedited, or metastasis inhibited.

Eukaryotic cells employ a variety of actin-based membrane protrusions to navigate their surroundings, including broad, sheet-like lamellipodia and slender filopodia (13–15). For generality, we abstract this taxonomy in what follows to consider a

general class of protrusions extended at the cell membrane that are used for both chemical gradient detection and the formation of focal adhesions with the extracellular matrix (ECM). In adhesion-dependent migration, nascent adhesions couple actin-based protrusions to the ECM, while actomyosin contractility and adhesion turnover coordinate cell-body translocation and rear retraction (16–18). When protrusive activity is chemotactically biased, these processes generate net migration along chemical gradients.

A poor mechanistic understanding of the factors driving cellular morphological variation motivates the search for a general organising principle linking cellular protrusive activity to the environmental conditions under which migration occurs. In this work, we use as a modelling hypothesis that, during chemotaxis, eukaryotic cells adopt protrusive phenotypes that maximise their energetic efficiency, which we define as the distance they migrate along a chemical gradient per unit of energy expended in gradient sampling (which yields information about the direction of the gradient) and movement. Such a principle is biologically well-motivated, in that actin remodelling and protrusion-mediated migration impose substantial energetic demands and mechanical confinement alters the energetic cost of cell migration (19–21). These observations, in turn, motivate an interrogation of whether energetic efficiency can serve as an organising principle for protrusive responses to environmental parameters. Formalising this hypothesis within a quantitative framework permits the derivation of the protrusive phenotype that maximises energetic efficiency under a given set of environmental conditions, and a systematic comparison of the resulting predictions with experimental observations across a range of biological systems.

The role of exogenous signals in protrusion formation is a point of controversy in the experimental literature (22). In traditional *chemotactic compass* models, ligand binding at cell surface receptors induces the formation of protrusions by activating intracellular signalling pathways, polarising cells in the direction of a chemical gradient (23, 24). Conversely, in *pseudopod-centred* models, *de novo* protrusions are formed at random positions along the cell membrane, and exogenous signalling subsequently stabilises, grows, and divides pseudopodia preferentially in regions of higher chemical concentration to polarise the cell (7, 12, 22). Experimental evidence supports elements of both of these hypotheses, which need not be mutually exclusive in that spontaneous or excitable protrusive activity can coexist with receptor-mediated directional bias (25). The model formulated in this work is compatible with either paradigm, requiring only that the resulting protrusive phenotype can be evaluated in terms of energetic efficiency.

Mathematical modelling offers a valuable complement to experimental methods, and models of cellular protrusions and motility span scales from single-filament dynamics to whole-cell behaviour (see (26–28)). Recent work has used mathematical modelling to predict pseudopod splitting strategies in shallow gradients (29) and optimal morphologies for chemotactic gradient detection (30). Related work has examined the energetic efficiency of whole-cell migration across physical environments (31). The model formulated here addresses the complementary question of how protrusion number and length jointly determine expected chemotactic displacement per unit energy expended on protrusion formation and cell-body translocation.

In what follows, we develop this framework by combining a simple two-dimensional model for chemotaxis with a model for the energy expended upon the extension of protrusions, based on linear elasticity theory. We then analyse this model, and the protrusive phenotype that maximises energetic efficiency, to predict the variation in protrusive activity in response to a range of environmental factors. Where possible, we compare our predictions with corresponding experiments and, where not, we provide hypotheses that may be tested with future experiments.

2 METHODS

We consider a cell of radius l_0 in the two-dimensional plane and represent its membrane as a closed one-dimensional elastic loop (32, 33). We wish to study the energy-motility trade-off in extending actin-rich protrusions at the cell membrane during chemotactic movement. In doing so, we begin by deriving expressions for the energetic costs of cell movement and protrusion formation, before constructing a simple two-dimensional model for chemotaxis, in which we relate the number and length of protrusions extended to the probability of chemical gradient detection and subsequent movement (Figure 1). In the following derivation, we consider cell movement up concentration gradients, though the model is straightforwardly adapted to consider the converse, which is also a well-documented mechanism of migration (e.g., in the migration of neutrophils (34)).

2.1 Energetic cost of cell movement

We begin by calculating the energetic cost of cell-body translocation during chemotaxis. For simplicity, we assume that the actin-based protrusions extended by a cell are all of equal length (l_p, say) and that they are extended instantaneously. We denote by E_m the energetic cost of translocating the cell body following protrusion-mediated sensing of the environment. The distinct energetic costs of forming the protrusions themselves are formulated in subsequent sections through membrane deformation and dissipation terms.

We consider a microenvironment in which the effective mechanical resistance encountered by the cell is spatially uniform,

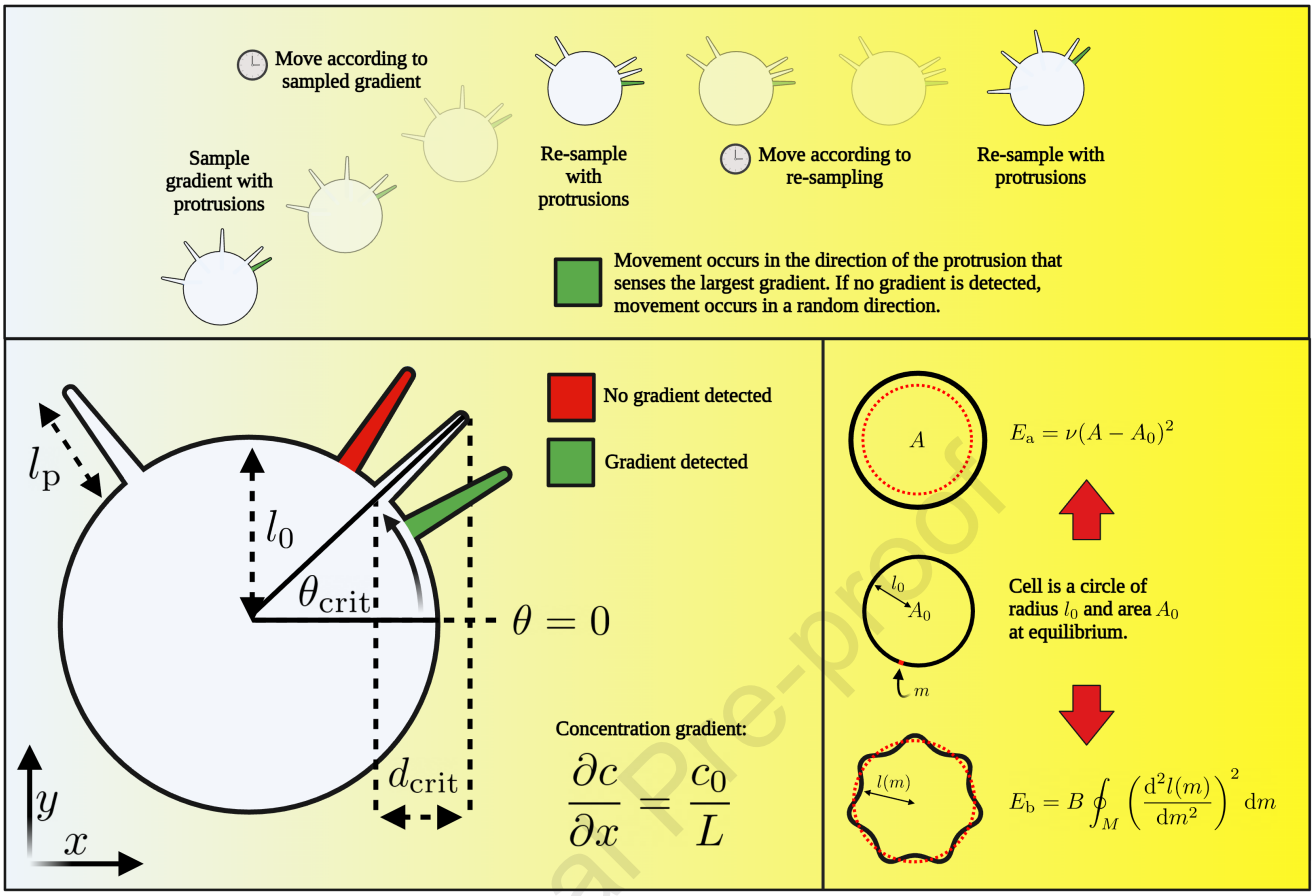

Figure 1: Schematic of the two-dimensional chemotaxis model and the energetic costs of protrusion extension. In the two-dimensional model of chemotaxis, a cell, initially of radius l_0, samples its environment with n_p protrusions at a discrete number of time points (upper panel). Each protrusion is of length l_p, and protrusions are oriented at angles $\{\theta_i\}$, sampled independently from an underlying distribution $f(\theta)$ for $\theta \in [0, \pi]$ (neglecting the lower half plane due to symmetry). If the smallest of the angles sampled, θ_{min}, satisfies $\theta_{min} \leq \theta_{crit}(l_p)$, then movement occurs in the direction of the protrusion extended at θ_{min}. If this condition is not met, then the cell moves in a random direction, such that its expected distance moved along the chemical gradient is zero. The energetic costs of membrane deformation are partitioned into an energy cost due to area change in the cell and an energy cost due to increased membrane curvature, such that all possible perturbations on the circle within the two-dimensional plane are penalised. Created in BioRender by Samuel W.S. Johnson: https://BioRender.com/kr8jhrj.

represented by a fixed value of the parameter β. This coarse-grained resistance may include contributions from substrate or matrix stiffness, friction, effective viscosity, adhesion strength, porosity, and matrix remodelling. If the effective resisting force opposing cell-body translocation is approximately constant during migration, then the mechanical work required to move a distance d is proportional to d. We write this effective resisting force as $\alpha_m\beta$, giving

$$E_m = \alpha_m \beta d, \tag{1}$$

where d is the total distance travelled between the extension and retraction of protrusions and α_m sets the energetic scale for movement per unit distance in a reference environment with $\beta = 1$. The two-dimensional model considered here should be understood as a two-dimensional representation of migration *through* a three-dimensional resistive microenvironment, with β encapsulating the frictional and adhesive coupling and other dissipative processes that resist cell-body translocation. Here, we note that if we were to instead model migration *on* a two-dimensional substrate, akin to many *in vitro* systems, much of the mechanical resistance to movement would be attenuated, with frictional forces dominating the mechanical energetic costs of movement.

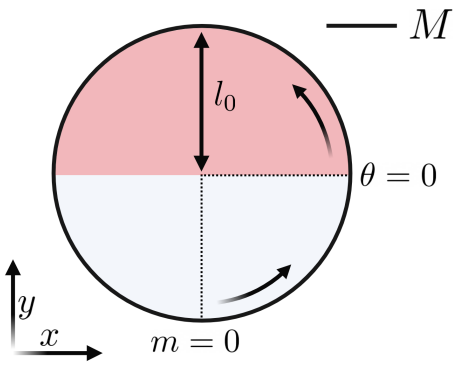

Figure 2: Schematic of the membrane coordinate system. $\theta = 0$ denotes the positive x-direction and corresponds to the point $m = \pi l_0/2$ on the membrane, M. Protrusions are formed in the upper half-plane (dashed red region) to prevent discontinuities at the endpoints of the membrane, $m = 0, P$. Created in BioRender by Samuel W.S. Johnson: https://BioRender.com/rpe6hx4.

2.2 Energetic cost of membrane bending

In calculating the energetic cost of protrusion extension, we adopt a framework similar to that of Ryan et al. (35) and decompose the mechanical energetic cost of extending actin-based protrusions into a cost due to the area change of a cell and a cost due to bending of the cell membrane. At equilibrium, we assume that the outward force from actin polymerisation inside the cell is balanced by a tensile force from the membrane. From force balance, we then calculate the mechanical energy expended in actin polymerisation as the energy to deform the cell membrane.

The cell membrane, initially taken to be circular with equilibrium radius l_0, is parametrised by a coordinate $m \in [0, P]$, where $P = 2\pi l_0$ is the initial circumference of the membrane. The coordinate m relates directly to the angular orientation θ around the cell, measured anticlockwise from a reference direction (chosen as $\theta = 3\pi/2$ at the bottom of the cell). Thus, we have

$$\theta = \left(\frac{m}{l_0} + \frac{3\pi}{2}\right) \bmod 2\pi. \tag{2}$$

To prevent discontinuities at the domain boundaries ($m = 0$ and $m = P$), we select this convention so that protrusions are formed away from $m = 0$ and $m = P$ (Figure 2).

When the cell membrane is deformed by extending a protrusion, its additional curvature relative to the circular reference state, C, at a point m_0 is given by

$$C(m_0) = \left.\frac{\mathrm{d}^2 l(m)}{\mathrm{d}m^2}\right|_{m=m_0}, \tag{3}$$

where $l(m) = l_0 + u_\mathrm{p}(m)$ is the radial distance from the cell centre to point m on the membrane. We assume that protrusions are sufficiently small, allowing local segments of the curved membrane to be approximated as linear. This simplification justifies taking derivatives directly with respect to the membrane coordinate m without explicitly including higher-order curvature corrections.

Under these assumptions, the potential energy associated with bending the membrane is defined as

$$E_\mathrm{b} = B \oint_M \left(\frac{\mathrm{d}^2 l(m)}{\mathrm{d}m^2}\right)^2 \mathrm{d}m, \tag{4}$$

where M is the cell membrane and B is an effective line-bending stiffness of the planar elastic loop (36).

For analytical simplicity, we model protrusions as Gaussian in shape, so that

$$l(m) = l_0 + l_\mathrm{p} \exp\left(-\left(\frac{m - m_\mathrm{c}}{w_\mathrm{p}}\right)^2\right), \tag{5}$$

where l_p and w_p represent the characteristic protrusion length and width, respectively, and m_c denotes the central location of the protrusion along the membrane.

Calculating the second derivative of $l(m)$ with respect to m indicates that the curvature induced by a protrusion scales linearly with the protrusion length l_p. Consequently, the bending energy per protrusion scales as $E_\mathrm{b} \sim l_\mathrm{p}^2$. Furthermore, for

well-spaced protrusions of equal length and width, the total bending energy increases linearly with the number of protrusions. Combining these scaling relations yields the total energetic cost associated with membrane bending due to n_p Gaussian protrusions, each of length l_p as

$$E_\mathrm{b} = \alpha_\mathrm{b} n_\mathrm{p} l_\mathrm{p}^2, \tag{6}$$

where α_b represents the energy required to extend a single protrusion of unit length.

2.3 Energetic cost of cell expansion

In calculating the energetic cost due to the change in area of a cell upon the extension of actin-based protrusions, we consider an expression that penalises both an increase and decrease in cell area relative to its equilibrium value

$$E_\mathrm{a} = \nu (A - A_0)^2, \tag{7}$$

where A is the area of a cell after the extension of protrusions, A_0 is the baseline area of the cell (its area when no protrusions are extended), and ν is an elastic constant of expansion and contraction associated with membrane tension. Here, we have taken the energetic cost to scale quadratically with an increase or decrease in cell area (and hence, cell strain to be sufficiently small such that the assumption of linear elasticity holds (32, 33)).

When a cell extends a protrusion of a fixed length and width, a constant value is added to the area of the cell (A_ϵ, say). Assuming that n_p protrusions of equal size are extended, the corresponding increase in area is given by $n_\mathrm{p} A_\epsilon$. The energetic cost resulting from the area change in a cell after the extension of n_p protrusions of equal size, therefore, scales as $E_\mathrm{a} \sim n_\mathrm{p}^2$. The area of a Gaussian protrusion scales linearly with its length (for a fixed characteristic width). Consequently, the energetic cost of the area change in a cell also scales quadratically with the length of the protrusions; $E_\mathrm{a} \sim l_\mathrm{p}^2$.

Combining the scaling relations for n_p and l_p, the total energetic cost of extending n_p protrusions, each of length l_p, is

$$E_\mathrm{a} = \alpha_\mathrm{a} n_\mathrm{p}^2 l_\mathrm{p}^2, \tag{8}$$

where α_a is the energetic cost due to cell expansion upon extending a single protrusion of unit length.

We henceforth interpret E_a as an effective, coarse-grained penalty for finite membrane extensibility and cell-shape change, rather than as a literal equilibrium pressure cost. On the timescales relevant to protrusive sampling, cell permeability and pressure equilibration through fluid flow may relax part of this deformation. Within the present framework this corresponds to a smaller effective value of α_a. As shown in Appendix A, the qualitative predictions of the model are robust to variation in α_a, such that this reinterpretation does not affect our conclusions in this work.

2.4 Dissipative cost of protrusion extension

Equations (1), (6), and (8) account for the reversible elastic deformation of the cell membrane and the mechanical work of cell-body translocation. The extension of an actin-based protrusion during chemotaxis is, however, an inherently dissipative process. The actin polymerisation that underpins the formation of protrusions is sustained by the irreversible hydrolysis of adenosine triphosphate (ATP) (37, 38), and the advancing membrane and filament network must continuously overcome viscous drag from the surrounding cytoplasm and the resistance of the polymerisation machinery itself (39, 40). A portion of the chemical energy supplied during protrusion is, therefore, dissipated rather than stored elastically.

We assume an effective dissipative cost that is proportional to the polymerised actin mass. For protrusions of a fixed characteristic width, this is proportional to the filament length, such that the dissipated energy of a single protrusion scales linearly with l_p. The other irreversible processes accompanying protrusive sampling share this scaling. For protrusions of a fixed characteristic width, filament assembly and retraction, the turnover of adhesions formed along the protrusion, local contractility, and the sensing cost of receptors distributed over the protrusion membrane each scale to leading order with the protrusive membrane generated, and hence with l_p. Consequently, for n_p protrusions of equal length extended in unison, the total dissipative cost is

$$E_\mathrm{d} = \alpha_\mathrm{d}\, n_\mathrm{p} l_\mathrm{p}, \tag{9}$$

where α_d is the effective free energy dissipated per unit protrusive length, aggregating the free energy of actin polymerisation together with the cost of filament assembly and retraction, adhesion turnover, local contractility, and gradient sensing during chemotactic gradient sampling.

2.5 Total energetic cost of chemotactic cell motility

Combining Equations (1), (6), (8), and (9), we obtain an expression for the total energy required for a cell to extend n_p protrusions, each of length l_p, and move a distance d in an ECM of effective resistance β as

$$E = E_\mathrm{b} + E_\mathrm{a} + E_\mathrm{m} + E_\mathrm{d} = \alpha_\mathrm{b} n_\mathrm{p} l_\mathrm{p}^2 + \alpha_\mathrm{a} n_\mathrm{p}^2 l_\mathrm{p}^2 + \alpha_\mathrm{d} n_\mathrm{p} l_\mathrm{p} + \alpha_\mathrm{m} \beta d. \tag{10}$$

2.6 Expected distance moved in chemotactic cell motility

We now proceed to formulate a simple two-dimensional representation of eukaryotic chemotaxis to calculate the expected distance moved in chemotaxis as a function of n_p and l_p (Figure 1). In defining a chemoattractant landscape, we consider a concentration profile in which the concentration of the chemical driving movement increases linearly with respect to x and with no dependency on y, such that $c(x, y) = c_0 x/L$. Limits on the accuracy with which cells can detect environmental gradients are well-studied (41). As such, we fix a threshold distance in the positive x direction, d_crit, which is the minimum distance between the base and the tip of a protrusion that must be spanned in the positive x-direction for a chemical gradient to be detected (in Figure 1, the green protrusion meets this condition, whereas the red protrusion does not). From the model geometry, d_crit, therefore, imposes a minimum concentration difference of $d_\mathrm{crit} c_0/L$ between the base and the tip of a protrusion, for a gradient to be detectable. The notion of a critical distance, d_crit, also affords the definition of a corresponding angle, $\theta_\mathrm{crit} = \cos^{-1}(d_\mathrm{crit}/l_\mathrm{p}) \in [0, \pi/2]$, which depends on the length of a protrusion l_p, and determines the maximum angle at which a protrusion can be extended such that a gradient is detected (note here that if $l_\mathrm{p} < d_\mathrm{crit}$, no such angle can be defined, meaning that a gradient is never detectable). We also assume that protrusions are extended perpendicular to the cell membrane and that the angles at which protrusions are extended are sampled independently from an underlying distribution, $f(\theta)$, for $\theta \in [0, \pi]$, where the lower half plane $\theta \in (\pi, 2\pi)$ is neglected due to up-down symmetry. Here, an angle of $\theta = 0$ corresponds to the extension of a protrusion in the positive x direction, while an angle of $\theta = \pi/2$ corresponds to the extension of a protrusion in the positive y direction. When a cell extends n_p protrusions, we assume that all protrusions are the same length and are instantaneously extended in unison (the relaxation of the assumption of equal length across protrusions is the subject of future work within the same framework). Furthermore, we prescribe cell movement in the direction of the protrusion that senses the highest environmental concentration gradient (from the geometry of the system, this corresponds to the protrusion extended at the angle closest to $\theta = 0$). If a gradient is not detected due to no protrusion spanning a sufficient distance in the positive x-direction, then the cell moves in a random direction. We now calculate the expected distance moved by a cell upon the extension of n_p protrusions of length l_p.

To calculate the probability of gradient detection in cell movement (the probability that at least one protrusion is extended at an angle lower than θ_crit in Figure 1), we derive the probability density function of the minimum angle of n_p samples from the distribution $f(\theta)$. For n_p independent samples from this distribution, the probability that all angles are greater than a value θ is given by

$$\left(1 - \int_0^\theta f(\theta')\mathrm{d}\theta'\right)^{n_\mathrm{p}}. \tag{11}$$

From this, the cumulative distribution function of the minimum of these n_p samples is given by

$$P(\theta) = 1 - \left(1 - \int_0^\theta f(\theta')\mathrm{d}\theta'\right)^{n_\mathrm{p}}. \tag{12}$$

Differentiating Equation (12) with respect to θ, the probability density function of the minimum angle sampled is

$$p(\theta) = n_\mathrm{p} f(\theta) \left(1 - \int_0^\theta f(\theta')\mathrm{d}\theta'\right)^{n_\mathrm{p}-1}. \tag{13}$$

From this expression, we obtain the probability of gradient detection upon the extension of n_p protrusions of length l_p as

$$\int_0^{\theta_\mathrm{crit}} p(\theta'')\mathrm{d}\theta'' = n_\mathrm{p} \int_0^{\theta_\mathrm{crit}} f(\theta'') \left(1 - \int_0^{\theta''} f(\theta')\mathrm{d}\theta'\right)^{n_\mathrm{p}-1} \mathrm{d}\theta'', \tag{14}$$

where θ_crit is the maximum angle for which a protrusion of length l_p can be extended such that a gradient is detected:

$$\theta_\mathrm{crit} = \cos^{-1}\left(\frac{d_\mathrm{crit}}{l_\mathrm{p}}\right). \tag{15}$$

We now calculate the expected distance travelled by a cell upon the extension of n_p protrusions of length l_p. If the smallest of the n_p angles sampled, θ_min, satisfies $\theta_\mathrm{min} \leq \theta_\mathrm{crit}$, the distance moved by a cell in the positive x direction (the direction of the environmental gradient) is given by

$$d\cos(\theta_\mathrm{min}), \tag{16}$$

where d is the distance moved by the cell upon the extension of protrusions. If the minimum orientation of n_p protrusions does not meet the threshold for gradient detection ($\theta_\mathrm{min} > \theta_\mathrm{crit}$), then movement is unbiased, and hence, vanishes under expectation. Consequently, the expected distance travelled by a cell in the direction of an environmental gradient upon extending n_p protrusions, each of length l_p, is obtained as

$$dn_\mathrm{p}\int_0^{\theta_\mathrm{crit}} f(\theta'')\cos(\theta'')\left(1-\int_0^{\theta''} f(\theta')\mathrm{d}\theta'\right)^{n_\mathrm{p}-1}\mathrm{d}\theta'', \tag{17}$$

where we have accounted for gradient-induced movement by integrating only from 0 to θ_crit.

A final consideration we make in the expression for distance moved is the effect of substrate resistance and organisation on the speed at which a cell can move (and hence, the distance moved between the extension and retraction of protrusions). In the model, we characterise the ECM in terms of its resistance to motion (β), and a parameter that we refer to as topographical permissibility (ϕ), which determines how permissive to cell migration the ECM is for a given value of β (and hence, is a parameter that captures properties such as the degree to which fibres in the ECM are aligned). We then define a function, $g(\beta,\phi)$, that modulates the distance moved by a cell between the extension and retraction of protrusions, and depends on the effective resistance (β) and topography (ϕ) of the surrounding ECM. Since $g(\beta,\phi)$ rescales the realised distance travelled per cycle from d to $g(\beta,\phi)d$, the associated translocation cost is correspondingly $\alpha_\mathrm{m}\beta g(\beta,\phi)d$ rather than $\alpha_\mathrm{m}\beta d$. As such, Equation (17) can be modified to account for substrate resistance and permissibility as

$$g(\beta,\phi)dn_\mathrm{p}\int_0^{\theta_\mathrm{crit}} f(\theta'')\cos(\theta'')\left(1-\int_0^{\theta''} f(\theta')\mathrm{d}\theta'\right)^{n_\mathrm{p}-1}\mathrm{d}\theta''. \tag{18}$$

At this point, we do not prescribe a functional form for $g(\beta,\phi)$, though in subsequent sections, we make phenomenological selections for $g(\beta,\phi)$ to study how substrate stiffness and topography affect protrusive activity in a range of biological scenarios.

2.7 Final expression for the expected distance travelled per unit energy expended in environmental sensing and cell movement

Combining Equations (10) and (18), we arrive at an expression for the expected distance, d_x, travelled up a fixed chemical gradient in chemotaxis per unit energy expended by a cell (E) upon the extension of n_p protrusions, each of length l_p, as

$$\frac{\mathbb{E}(d_x)}{E} = \frac{g(\beta,\phi)dn_\mathrm{p}\int_0^{\theta_\mathrm{crit}} f(\theta'')\cos(\theta'')\left(1-\int_0^{\theta''} f(\theta')\mathrm{d}\theta'\right)^{n_\mathrm{p}-1}\mathrm{d}\theta''}{\alpha_\mathrm{b}n_\mathrm{p}l_\mathrm{p}^2+\alpha_\mathrm{a}n_\mathrm{p}^2l_\mathrm{p}^2+\alpha_\mathrm{d}n_\mathrm{p}l_\mathrm{p}+\alpha_\mathrm{m}\beta g(\beta,\phi)d}. \tag{19}$$

Without loss of generality, Equation (19) may be simplified by fixing $\alpha_\mathrm{b}=1$ and rescaling all other terms in Equation (19), such that

$$\frac{\mathbb{E}(d_x)}{E} = \frac{g(\beta,\phi)dn_\mathrm{p}\int_0^{\theta_\mathrm{crit}} f(\theta'')\cos(\theta'')\left(1-\int_0^{\theta''} f(\theta')\mathrm{d}\theta'\right)^{n_\mathrm{p}-1}\mathrm{d}\theta''}{n_\mathrm{p}l_\mathrm{p}^2+\alpha_\mathrm{a}n_\mathrm{p}^2l_\mathrm{p}^2+\alpha_\mathrm{d}n_\mathrm{p}l_\mathrm{p}+\alpha_\mathrm{m}\beta g(\beta,\phi)d}. \tag{20}$$

We henceforth refer to Equation (20) as the distance-to-energy ratio (DTER) of cell movement.

2.8 Scope of the DTER model assumptions

We defer an extended discussion of the assumptions used to derive Equation (20) to Appendix B, where we summarise their interpretation and possibilities for future relaxation. Here, we note that the model should be interpreted as a coarse-grained energetic framework for comparing protrusive phenotypes rather than a detailed mechanistic description of protrusion assembly and subsequent cell movement.

3 RESULTS

We now analyse the model as defined in Equation (20) to study the variation in the optimum protrusive phenotype (the combination of n_p and l_p that maximises the DTER), as a function of various environmental parameters and cellular behaviours.

3.1 Shallow chemical gradients drive a transition from bet-hedging to speculative phenotypes

The first parameter we consider in the study of Equation (20) is the threshold distance for the detection of a chemical gradient by the cell, d_crit. This parameter can be thought of as representing the steepness of the chemical gradient in the domain, with higher threshold distances representing a shallower chemical gradient as protrusions must span a larger distance for a gradient to be detected.

In analysing the effect of d_crit on the optimal protrusive phenotype, we take $f(\theta)$, the probability distribution that governs the orientation of the protrusions extended at the cell membrane, to be the uniform distribution $\mathrm{U}[0,\pi]$, such that

$$f(\theta) = \frac{1}{\pi}. \tag{21}$$

This form of $f(\theta)$ represents unbiased independent protrusion generation, where the generation of actin-driven protrusions is independent of the environmental chemical landscape within which a cell is positioned. However, we will later consider biases in this probability distribution, to compare the pseudopod-centred model with traditional chemotactic compass models (Section 3.4).

In selecting $g(\beta,\phi)$, we again choose a phenomenological expression that penalises movement in substrates of extreme stiffness, and for which the topographical permissibility, ϕ, linearly increases the distance moved by a cell per unit of time. In very soft substrates, cells cannot generate sufficient traction forces for movement (42). In contrast, on substrates of very high resistance, cell motility is impeded by the physical barrier of the dense substrate (43). A functional form of $g(\beta,\phi)$ that satisfies these constraints is

$$g(\beta,\phi) = \frac{\phi\beta}{k}\exp\left(-\left(\frac{\beta}{k}\right)^2\right), \tag{22}$$

which peaks at an intermediate resistance of $\beta = k/\sqrt{2}$. With these two assumptions, Equation (20) becomes

$$\frac{\mathbb{E}(d_x)}{E} = \frac{\phi\beta d n_\mathrm{p}}{k\pi}\frac{\exp\left(-\left(\frac{\beta}{k}\right)^2\right)\int_0^{\theta_\mathrm{crit}}\cos(\theta'')\left(1-\frac{\theta''}{\pi}\right)^{n_\mathrm{p}-1}\mathrm{d}\theta''}{n_\mathrm{p}l_\mathrm{p}^2 + \alpha_a n_\mathrm{p}^2 l_\mathrm{p}^2 + \alpha_d n_\mathrm{p} l_\mathrm{p} + \alpha_\mathrm{m}\beta\left(\frac{\phi\beta}{k}\exp\left(-\left(\frac{\beta}{k}\right)^2\right)\right)d}. \tag{23}$$

In the absence of experimental parameterisation, we set the parameters α_a, α_m, α_d, and ϕ to unity and select values of $\beta = 5\times10^2$ and $k = 5\sqrt{2}\times10^2$ that constrain the optimum values of n_p and l_p to lie between 1 and 10 for the parameter ranges considered. However, in Appendix A, we discuss the results of a general model parameter sweep to study the effect of each parameter choice on the optimal values of n_p and l_p.

Varying the threshold distance protrusions must span in the direction of the environmental gradient reveals a transition between phenotypes as chemical gradients become increasingly shallow (Figure 3). For low values of d_crit (i.e. steep chemoattractant gradients), the optimum protrusive phenotype is one in which cells extend multiple short protrusions. Only short protrusions are required due to easily detectable chemical gradients, and multiple protrusions are extended to ensure that the direction of movement is optimised with respect to chemical gradients. In contrast, in shallow gradients, where long protrusions must be extended in order to detect a chemical gradient, the optimum number of protrusions to extend is $n_\mathrm{p} = 1$, due to the energetic costs of extending increasingly longer protrusions. This result highlights two distinct strategies for gradient detection, *bet-hedging* phenotypes, wherein risk is spread across multiple directions and *speculation* in shallow gradients, wherein all risk is placed in sampling a single direction.

In vivo experimental evidence for the transition between speculation and bet-hedging (Figure 3) lies in the cranial neural crest, wherein streams of cells migrate collectively, guided by external gradients in vascular endothelial growth factor (VEGF) (44). *In vivo*, the morphology of cranial neural crest cells varies along streams (45). At the leading edge of streams, where gradients in VEGF are steep, cranial neural crest cells adopt 'hairy' phenotypes, with multiple protrusions extended in many different directions. At the back of streams, where gradients in VEGF are extremely shallow, cells instead adopt 'bipolar' phenotypes, becoming highly polarised and extending few, long protrusions.

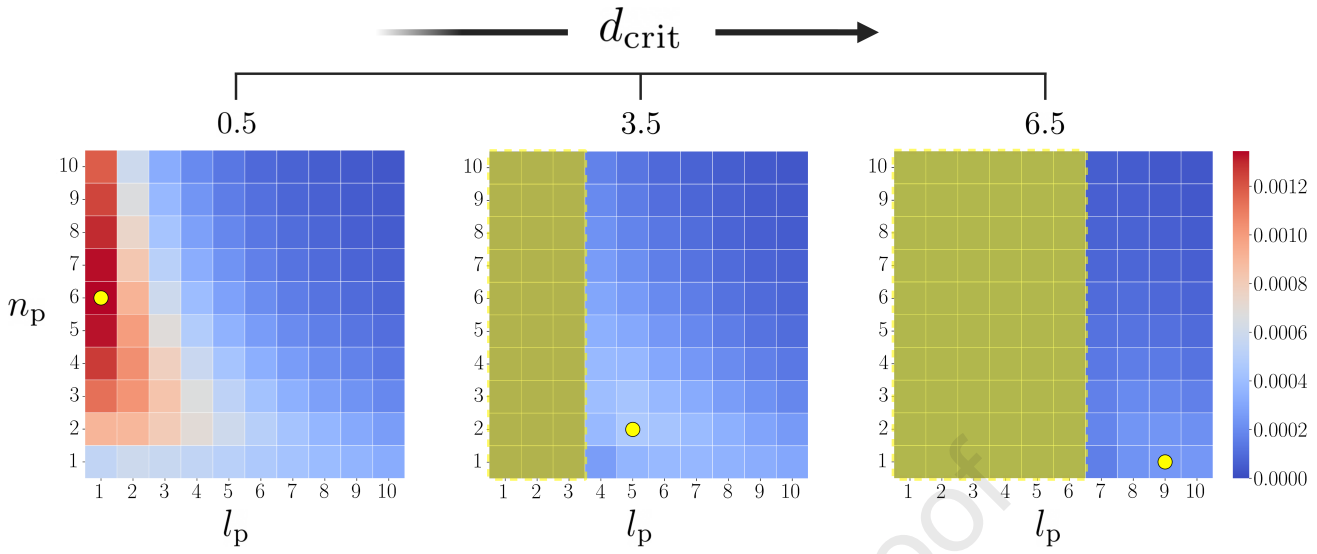

Figure 3: Heatmaps showing the evolution of the DTER with respect to d_{crit} (the steepness of the chemical gradient within the domain). When $d_{\mathrm{crit}} = 0.5$, the chemical gradient within the domain is of a large magnitude, such that the optimal strategy (yellow dot) is to sample multiple directions with short protrusions. Shaded yellow regions show parameter values in which gradient detection is not possible ($d_{\mathrm{crit}} > l_{\mathrm{p}}$). As d_{crit} is increased towards $d_{\mathrm{crit}} = 6.5$, representing increasingly shallower chemical gradients, the optimal strategy shifts to the extension of a lower number of protrusions, each of a longer length. All figures show numerical solutions of Equation (20) with $\alpha_{\mathrm{m}} = \alpha_{\mathrm{a}} = \alpha_{\mathrm{d}} = \phi = d = 1$, $\beta = 5 \times 10^2$, and $k = 5\sqrt{2} \times 10^2$.

However, in other contexts, the converse is true and cells in steeper chemical gradients exhibit enhanced polarity (e.g. in endothelial cells exposed to gradients in VEGF (46)). One possible reconciliation of this apparent discrepancy is to consider the distance travelled by neural crest cells relative to that of other migratory cell populations. *In vivo*, cranial neural crest cells must travel distances upwards of 1000 μm to colonise the branchial arches and facilitate proper facial patterning (47). Neural crest cells are among the most extensively migrating cell populations in the vertebrate embryo (48), and as such, energetic constraints in gradient detection may be more of a consideration for neural crest cells than the other cell types studied in this context, for which the rapid detection of gradients and subsequent migration may be prioritised (e.g. in wound healing).

3.2 Cell spreading exhibits a biphasic relationship with substrate stiffness

In Equation (23), the effective mechanical resistance of the substrate through which migration occurs is represented by the parameter β. As discussed in Section 2, β aggregates several mechanical properties of the cellular microenvironment. In this section, we take substrate stiffness to be its dominant, experimentally accessible determinant, and refer to variation in β as variation in stiffness for concreteness. The parameter ϕ captures all properties of the substrate that modify a cell's capacity for motility but do not affect the energetic cost of movement through the domain (e.g. the degree of fibre alignment in the ECM). Within this framework, we assume that a denser or stiffer microenvironment incurs an increased energetic cost of movement in cells and also that substrate stiffness modulates the distance moved in chemotactic cell motility due to a variation in the traction force a cell can generate and the mechanical impedance of cell movement in stiff substrates. Here, we fix β to be constant within the domain, and hence, such that the stiffness of the substrate is independent of the movement stimulus concentration profile.

We now study the effect of substrate topography on cell morphology by studying the protrusive strategies that maximise the DTER for a range of substrate stiffnesses, β, and substrate permissibilities, ϕ. As in Section 3.1, we assume that the distribution governing the orientation of protrusions is the uniform distribution, $\mathrm{U}[0, \pi]$, and that the parameters β and ϕ influence motility according to Equation (22). In the absence of experimentally-informed model parameterisation, we again fix the energetic parameters α_{a} and α_{d} at unity, and systematically vary β and ϕ, representing a progressive stiffening and aligning of the ECM.

Figure 4 shows that protrusive activity is maximised for intermediate values of β, where the distance migrated between sampling times is maximised. Furthermore, increasing ϕ increases the optimal value of n_{p} monotonically. This suggests that optimal protrusive activity in migration is linked to the motile capacity of cells, as determined by the substrate stiffness and topography. This, in turn, suggests that for migration through substrates *in vivo*, cells encountering highly aligned fibre networks and optimal stiffness can harness increased motility to extend numerous protrusions, thereby sampling their surroundings

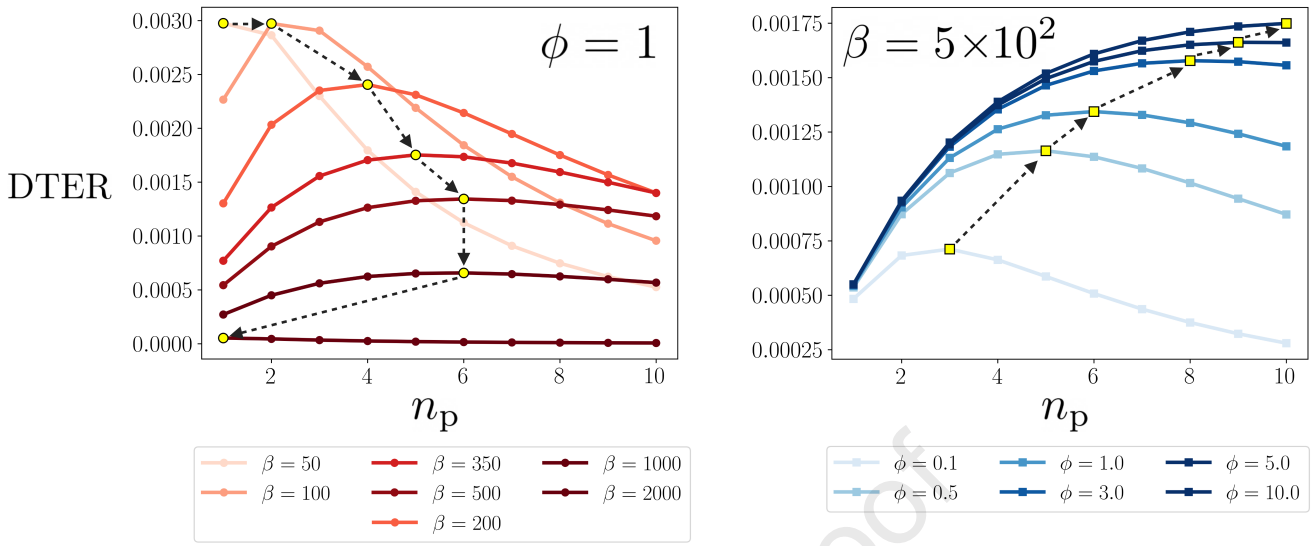

Figure 4: DTER as a function of n_p for a range of values of β and ϕ ($\alpha_a = \alpha_m = \alpha_d = 1, d_{crit} = 0.5, l_p = 1, k = 5\sqrt{2}\times10^2$). For low substrate stiffnesses (small values of β), model predictions suggest that the optimum number of protrusions to extend is $n_p = 1$. As substrate stiffness, β, is increased, the DTER is optimised for larger values of n_p. For very large substrate stiffnesses, the optimum value of n_p peaks, and subsequently decreases back to a value of $n_p = 1$. Increasing ϕ increases the optimum value of n_p monotonically. Yellow markers indicate the value of n_p^{opt} and arrows connect successive values of n_p^{opt} as β and ϕ are increased.

extensively and maintaining directional persistence along environmental concentration gradients. Conversely, in regions where the ECM is either too compliant or overly rigid, such as loosely organised interstitial spaces or densely cross-linked fibrotic tissue, cells may reduce protrusive sampling, favouring a minimal number of projections to conserve energy. These results reconcile conflicting trends observed *in vitro*, where in some cases, a stiffening of three-dimensional substrates causes enhanced cell spreading (49), whereas in other studies, the converse is true (50). The findings presented here suggest that these experiments may be sampling distinct regions of the biphasic dashed β-varying trajectory in Figure 4, and hence, observing opposing relationships between substrate stiffness and cell spreading. In both cases, if a wider range of stiffnesses were considered, our analysis predicts that the biphasic relationship predicted here would be observed.

The results presented in this section, therefore, suggest that substrate topography is a major determinant of protrusive activity in motile cells, and that this relationship may be understood through the trade-off in the energy expended in environmental sampling and the distance moved upon sampling. In overly stiff or compliant substrates, the distance moved through the substrate upon sampling is minimal, such that additional protrusions confer little motility benefit but incur a high energetic cost. Conversely, when the matrix composition is of an intermediate stiffness, allowing for longer migratory distances between sampling, cells can afford to generate, and indeed benefit from extensive exploratory protrusions. If a cell is poised to travel a greater distance, it is energetically favourable to optimise the direction of movement by deploying numerous projections to accurately map out the local chemoattractant profile, thus increasing the likelihood of movement in the direction of the external chemical gradient.

The stiffness-dependent protrusion dynamics predicted by the model also raise intriguing questions about how cancer cells exploit invadopodia (51) and matrix metalloproteinases (MMPs) (52) to tune their own effective substrate mechanics. Invadopodia are actin-rich, protease-laden projections that locally degrade the ECM via MMP secretion. A coupling between protrusion density along the cell membrane and ECM degradation suggests the existence of a feedback loop between protrusive activity and substrate stiffness, wherein malignant cells extend invadopodia to degrade overly stiff substrates, and hence increase their motile capacity, which in turn, changes the optimal protrusive activity predicted by the model considered here. When stiffness is locally decreased to lie within the mechanical window that optimises motile capacity, cells may then downregulate invadopodia formation to conserve resources while maintaining exploratory protrusions for chemoattractant sampling. In contrast, when the ECM falls below the lower stiffness threshold, proteolysis would compromise traction forces and impede movement by further softening the substrate, such that cells may suppress invadopodia, yet continue to deploy non-proteolytic protrusions to survey their surroundings. Embedding this antagonistic regulation, where β and ϕ dynamically evolve in response

to MMP-mediated remodelling and protrusive sampling, into the DTER framework may capture how cancer cells iteratively sculpt their microenvironment, balancing ECM proteolysis and motility energetics to carve permissive invasion tracks and maximise invasive potential in mechanically heterogeneous tissues.

In addition to modulating local stiffness, MMP activity mobilises matrix-sequestered growth factors and chemoattractants (53), thereby establishing steep concentration gradients that can bias protrusion density and orientation. Such biochemical release mechanisms introduce an additional layer of protrusive regulation, operating in parallel with stiffness-dependent feedbacks to shape migratory dynamics. Invadopodia, therefore, function as structures that modify both the mechanical compliance of the ECM and the distribution of guidance cues in the surrounding microenvironment. Extending the DTER framework to include these coupled mechano-chemical interactions would enable analysis of how cancer cells synchronise proteolytic remodelling and chemotactic sampling to optimise invasion strategies.

3.3 Integration of signals between actin-based protrusions is optimal in well-sampled environments

In many eukaryotic cell types, there is evidence for signal integration across the cell membrane (54), such that chemotactic steering may be achieved not only by considering gradients detected by individual protrusions, but also by the integration of signals across the cell membrane to compare chemoattractant concentrations sampled at different receptor sites (55–57). In the context of the model considered here, this suggests an alternative model of environmental sampling, wherein the detection of a chemical gradient depends not on the concentration difference measured by an individual protrusion, but rather on the *total* concentration difference spanned by a cell upon the extension of multiple protrusions. In this section, we formalise this notion in terms of the model by defining

$$\theta_{\min} = \min_{1\le i\le n_{\mathrm{p}}} \theta_i, \qquad \theta_{\max} = \max_{1\le i\le n_{\mathrm{p}}} \theta_i. \tag{24}$$

The tip of each protrusion of length l_{p} measures the chemoattractant concentration at a distance $(l_0 + l_{\mathrm{p}})\cos(\theta_i)$ in the direction of the gradient relative to the centre of the cell, where θ_i is the orientation of protrusion i. As such, the maximum distance spanned in the x-direction by the tips of any two protrusions is given by

$$d_{\mathrm{int}} = (l_0 + l_p)(\cos(\theta_{\min}) - \cos(\theta_{\max})). \tag{25}$$

As before, we assume that upon the extension of n_{p} protrusions at the cell membrane, the orientations of the protrusions are determined by independent samples from the angular distribution $f(\theta)$;

$$\{\theta_i\}_{i=1}^{n_{\mathrm{p}}} \overset{\text{i.i.d.}}{\sim} f(\theta), \quad \theta \in [0,\pi]. \tag{26}$$

Writing the cumulative distribution function for $f(\theta)$ as

$$F(\theta) = \int_0^{\theta} f(\phi)\,\mathrm{d}\phi, \tag{27}$$

the joint probability density function of the smallest and largest orientations may be expressed as

$$p_2(\theta_{\min},\theta_{\max}) = n_{\mathrm{p}}(n_{\mathrm{p}}-1)\left[F(\theta_{\max}) - F(\theta_{\min})\right]^{n_{\mathrm{p}}-2} f(\theta_{\min})\, f(\theta_{\max}), \quad 0 \le \theta_{\min} < \theta_{\max} \le \pi, \tag{28}$$

where $n_{\mathrm{p}}(n_{\mathrm{p}}-1)$ counts the choices of which two samples attain the minimum and maximum, $f(\theta_{\min})$ and $f(\theta_{\max})$ are the endpoint densities, and $\left[F(\theta_{\max}) - F(\theta_{\min})\right]^{n_{\mathrm{p}}-2}$ is the probability that the remaining $n_{\mathrm{p}} - 2$ samples lie within $(\theta_{\min},\theta_{\max})$. Now, rather than requiring the x-component of one protrusion to exceed a fixed detection length, we instead impose a thresholding condition by requiring the difference in these projections to exceed a threshold distance, d_{crit},

$$d_{\mathrm{int}} \ge d_{\mathrm{crit}}, \tag{29}$$

where d_{int} is the maximum distance in the x-direction spanned by the tips of any two protrusions, as defined in Equation (25) and visualised in Figure 5(a).

If this condition holds, then the cell moves a distance d in the direction of the leading protrusion ($\theta_{\min}$), otherwise its expected drift vanishes (Figure 5(a)). From this, the expected drift in the x-direction upon the extension of protrusions is given by

$$\mathbb{E}[d_x^{\mathrm{int}}] = dg(\beta,\phi) \int_0^{\pi}\int_{\theta_{\min}}^{\pi} \cos(\theta_{\min})\; 1_{\{\,(l_0+l_{\mathrm{p}})(\cos(\theta_{\min})-\cos(\theta_{\max}))\ge d_{\mathrm{crit}}\}}\; p_2(\theta_{\min},\theta_{\max})\;\mathrm{d}\theta_{\max}\,\mathrm{d}\theta_{\min}. \tag{30}$$

In comparing this sampling strategy with the original sampling strategy defined in Section 2, we consider the fraction

$$\frac{\mathbb{E}[d_x]}{\mathbb{E}[d_x^{\text{int}}]} = \frac{n_{\text{p}} \int_0^{\theta_{\text{crit}}} f(\theta'') \cos(\theta'') \left(1 - \int_0^{\theta''} f(\theta') \mathrm{d}\theta'\right)^{n_{\text{p}}-1} \mathrm{d}\theta''}{\int_0^{\pi} \int_{\theta_{\text{min}}}^{\pi} \cos(\theta_{\text{min}}) \; 1_{\{(l_0+l_{\text{p}})(\cos(\theta_{\text{min}})-\cos(\theta_{\text{max}})) \geq d_{\text{crit}}\}} \; p_2(\theta_{\text{min}}, \theta_{\text{max}}) \; \mathrm{d}\theta_{\text{max}} \, \mathrm{d}\theta_{\text{min}}}, \tag{31}$$

which computes the ratio of expected distances moved in the positive x-direction in both of the sampling mechanisms considered here for a fixed n_{p} and l_{p}. In order to compare the relative efficacy of these two mechanisms, we perform a parameter sweep over n_{p}, l_{p}, and d_{crit} to determine the contexts in which either of these two mechanisms are optimal. In the following analysis, we once again assume that the angular distribution, $f(\theta)$, is the uniform distribution $\mathrm{U}[0, \pi]$.

The model reveals a consistent pattern across a range of chemoattractant threshold distances. When cells extend only a few long protrusions, the original single-protrusion measurement mechanism outperforms the signal integration mechanism in terms of expected forward drift per unit of energy expended (Figure 5(b)). In this regime, there is a moderate probability of any given protrusion spanning the threshold distance in the positive x-direction. However, even if multiple protrusions individually meet this thresholding condition, it may still be the case that the distance between the tips of any two protrusions does not. Furthermore, even if all protrusions are extended in the negative x-direction, a positive concentration difference may be detected between the tips of two protrusions, leading to movement down chemical concentration gradients. By contrast, when cells deploy many shorter protrusions, it is unlikely that a single protrusion individually meets the thresholding condition, but it is very likely that, of the many protrusions extended, the tips of the protrusions extended at the smallest and largest angles span a distance greater than d_{crit}, and that the smallest angle (which we assume determines the direction of movement) points in the approximate direction of the concentration gradient.

Placing these findings in a biological context suggests that cell-type–specific protrusive strategies may reflect adaptations to distinct migratory challenges. Cells such as neural crest or invasive carcinoma that probe dense matrices with a small number of long filopodia likely benefit from a single-protrusion detection mechanism, enabling them to migrate towards distant targets once an individual protrusion measures a chemoattractive gradient. In contrast, fibroblasts migrating in complex microenvironments extend numerous pseudopodia and lamellipodia that are distributed broadly over the leading edge. In such a regime, gradient sensing cannot rely on any single protrusion; instead, the cell may integrate signals across many simultaneously extended tips. In this context, signal integration may help to suppress stochastic fluctuations measured by individual protrusions and stabilise migration in shallow or noisy chemoattractant fields.

3.4 Angular bias in protrusion orientation is optimal in both noise-free and noise-perturbed landscapes

We now study the effect of varying the underlying angular distribution for protrusions, $f(\theta)$, and its relation to the optimal number and length of protrusions extended. In many migrating cell types, the biochemical and mechanical processes that govern actin dynamics are non-uniform around the cell membrane and are biased towards the front by polarity signalling pathways (for example, localised PI3K activation (58) or Rac-driven Arp2/3 recruitment (59)). This forward bias in protrusion orientation, whether arising from pre-existing polarity cues, membrane tension gradients, or feedback from nascent adhesions, can dramatically reshape the optimal trade-off between protrusion number and size. In shallow or noisy gradients, a strongly front-focused strategy may be too rigid, causing the cell to overlook off-axis cues that would otherwise steer it back on course. In contrast, in steep, well-defined gradients, a tight angular focus minimises wasted energy on poorly-oriented protrusions, allowing the cell to invest energy in fewer, longer extensions and thereby move more efficiently.

In order to study these effects within the model, we begin by considering

$$f(\theta; \kappa) = \frac{\exp\big(\kappa \cos(\theta)\big)}{\int_0^{\pi} \exp\big(\kappa \cos(\phi)\big) \, \mathrm{d}\phi} := \frac{\exp\big(\kappa \cos(\theta)\big)}{\pi \, I_0(\kappa)}, \qquad \theta \in [0, \pi], \tag{32}$$

such that the angles at which protrusions are generated are sampled independently from a von Mises distribution supported on $[0, \pi]$, with κ determining the bias with which protrusions are formed in the positive x direction ($\theta = 0$, the direction of the positive chemoattractant gradient in the model).

By fixing α_{a}, α_{m}, α_{d}, β, $g(\beta, \phi)$, and d in Equation (20), maximisation of the DTER for a given n_{p} and l_{p} simply means the maximisation of

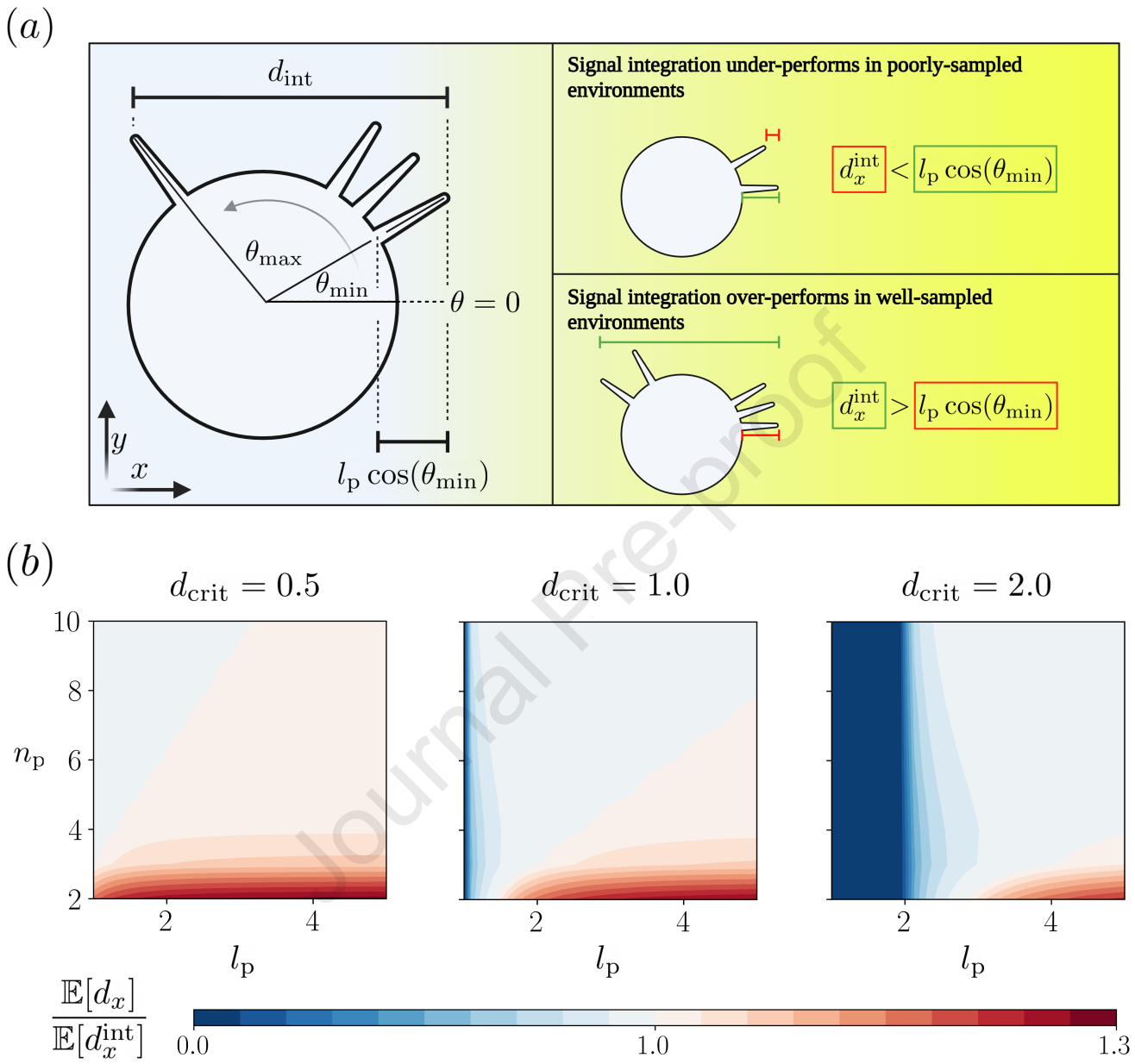

Figure 5: **(a)** Schematic of the original sensing mechanism and the protrusion-integrated sensing mechanism. In the original mechanism, a chemical gradient is detected if the protrusion extended at the lowest angle (θ_{min}) spans a sufficient distance in the positive x-direction. In the integrated sensing mechanism, a gradient is detected if the tips of the protrusions extended at the smallest and largest angles (θ_{min} and θ_{max}) span a sufficient distance in the x-direction ($d_{\text{int}} \geq d_{\text{crit}}$). Model analysis shows that when the local environment is well-sampled (i.e. n_{p} is sufficiently high), the integrated sensing mechanism outperforms the single-protrusion sensing mechanism. Conversely, when the environment is poorly-sampled, the original single-protrusion detection mechanism outperforms signal integration for sufficiently large values of l_{p}. **(b)** Heatmaps of the ratio of the expected distances moved under the single-protrusion and integrated sensing mechanisms, computed for three detection thresholds ($d_{\text{crit}} = 0.5, 1.0, 2.0$). Note that the colour bar uses a different linear scale below and above 1 (i.e. across the intervals [0, 1] and [1, 1.3]). The schematic in **(a)** was produced in BioRender: https://BioRender.com/r68g480.

$$\int_0^{\theta_{\text{crit}}} f(\theta'', \kappa)\cos(\theta'')\left(1 - \int_0^{\theta''} f(\theta', \kappa)\mathrm{d}\theta'\right)^{n_\text{p}-1} \mathrm{d}\theta'', \tag{33}$$

with respect to κ. In chemoattractant profiles with a noise-free gradient in the x direction ($c(x, y) = c_0 x/L$), it is trivial to see that increasing κ increases the DTER monotonically as, in this idealised situation, efficient movement simply means the minimisation of θ_{min} (such that the largest possible gradient is detected, and movement is optimised to occur in the direction of the gradient).

For migration *in vivo*, a more pertinent question is whether the same relationship holds in more realistic chemoattractant profiles where the chemoattractant landscape is perturbed with spatially-correlated noise. In order to probe how environmental heterogeneity alters the optimal angular bias, we superimpose a spatially-correlated noise field $\eta(x, y)$ onto the idealised gradient considered previously. Specifically, we define

$$c(x, y) \;=\; \frac{c_0}{L}\, x \;+\; \sigma\, \eta(x, y), \tag{34}$$

where η is drawn from a Gaussian random field with zero mean, unit variance, and squared-exponential covariance

$$\mathbb{E}\big[\eta(\mathbf{r})\,\eta(\mathbf{r}')\big] = \exp\!\Big(-\|\mathbf{r} - \mathbf{r}'\|^2/4\xi^2\Big), \tag{35}$$

where $\mathbf{r} = \mathbf{r}(x, y)^\top$ and ξ is a parameter that determines the correlation length of the noise field. The noise amplitude, σ, therefore sets the signal-to-noise ratio (SNR) of the local gradient cues. In order to study the chemoattractant landscape in Equation (34), we now re-cast the DTER model as a stochastic agent-based model (ABM).

We simulate cell migration in a noisy chemoattractant landscape using an ABM with discrete protrusive sampling. The two–dimensional concentration field is defined on a square domain of side length L, with $\eta(x, y)$ and σ as defined above. The field is generated by sampling white noise on an $N \times N$ grid, convolving with a Gaussian kernel of width ξ, rescaling to standard deviation σ, and adding the linear gradient of slope c_0/L.

At each discrete time, t, the cell is treated as a point particle at position $\mathbf{X}_t$ and draws n_p protrusion angles $\{\theta_i\}$ from a von Mises distribution $f(\theta; \kappa)$ centred on the positive x-direction, $\theta = 0$. For each protrusion, i, at time t, the tip location is computed as

$$\mathbf{X}_t^{(i)} = \mathbf{X}_t + l_\text{p}[\cos(\theta_i), \sin(\theta_i)]^T, \tag{36}$$

and the concentration difference as $\Delta c_i = c(\mathbf{X}_t^{(i)}) - c(\mathbf{X}_t)$. A detection threshold $\Delta c_{\text{crit}} = (c_0/L)\, d_{\text{crit}}$ is imposed, and the set $\mathcal{M} = \{\, i : \Delta c_i \geq \Delta c_{\text{crit}}\}$ is formed. If $\mathcal{M}$ is empty, the cell moves a distance d in a random direction, otherwise it selects $i^* = \arg\max_{i\in\mathcal{M}} \Delta c_i$ and moves according to

$$\mathbf{X}_{t+1} = \mathbf{X}_t + d[\cos(\theta_{i^*}), \sin(\theta_{i^*})]^T. \tag{37}$$

After T steps the net displacement $\Delta\mathbf{X} = \mathbf{X_T} - \mathbf{X}_0$ is recorded, and over M independent realisations of the landscape and trajectory we compute the mean of $\Delta\mathbf{X}$. By fixing n_p, l_p, β, and d_{crit} (and hence, the energy expended in environmental sampling and movement), we vary κ, σ, and ξ to quantify how protrusion directional bias influences chemotactic efficiency for a range of background environmental noises and correlation lengths.

The analysis in Figure 6 shows that increasing the bias parameter κ (i.e. imposing a stronger front-focused bias on protrusion orientation) yields a monotonic improvement in chemotactic efficiency in noise-perturbed chemical landscapes. By concentrating sampling in the direction of the global concentration gradient, cells reduce energy wasted on off-axis protrusions and maximise net forward displacement per unit energy.

However, as the characteristic length-scale of spatially correlated noise is increased, the benefit of angular bias is somewhat attenuated. When the noise correlation length (i.e. the distance over which correlations are reduced by a factor of e), 2ξ, is much smaller than the protrusion length, $l_\text{p} = 5$, local fluctuations decorrelate over distances shorter than the sampling scale, such that spurious peaks and troughs in the chemical concentration average out across tips and the underlying linear gradient dominates. In this regime, a strong front-focused bias ($\kappa \gg 1$) yields maximal chemotactic efficiency. As the correlation length grows to be comparable to l_p, however, the noise becomes coherent across neighbouring protrusions; multiple tips sample the same short-range gradient, which can mask or reverse the true global chemoattractant gradient. This reduces the net benefit of angular bias and can even make intermediate bias optimal. Finally, for sufficiently large correlation lengths, the noise field appears nearly constant over each cell's sampling region, merely shifting the concentration baseline without creating misleading local gradients, so that again a strong angular bias best leverages the true signal.

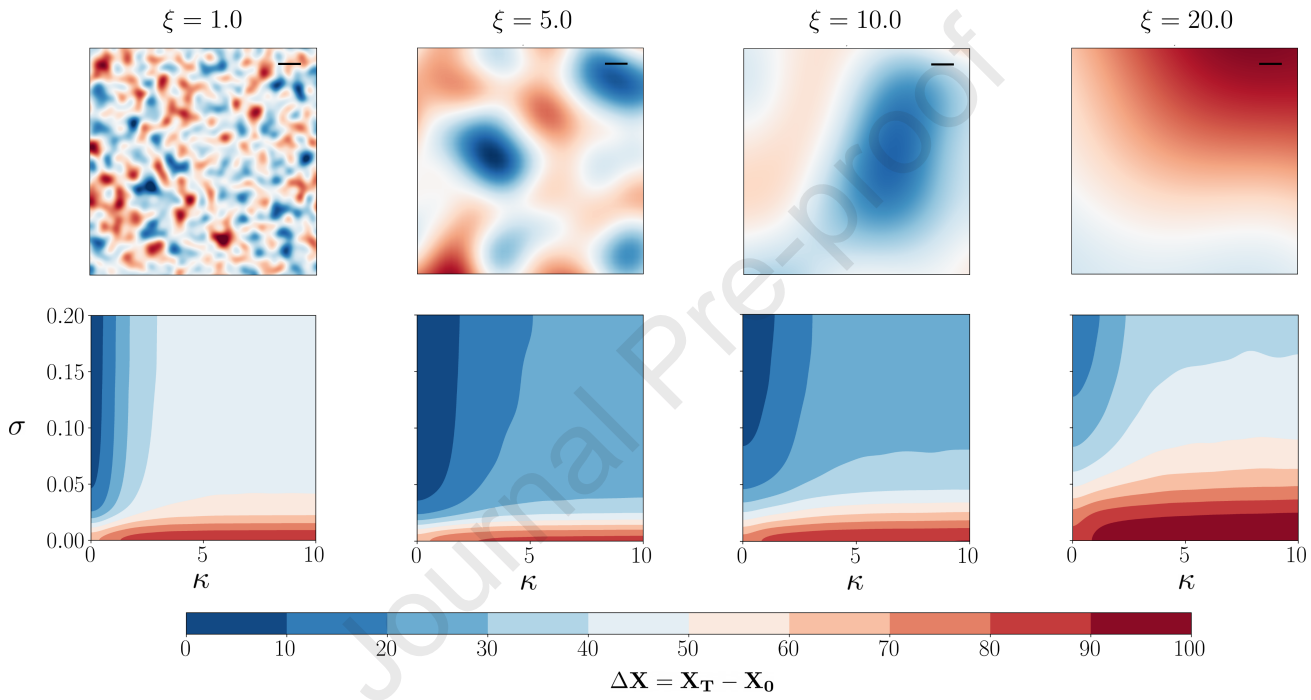

Figure 6: Heatmaps of mean displacement $\langle \Delta \mathbf{X} \rangle$ as a function of environmental noise σ and protrusion orientation bias κ, for correlation parameters $\xi = 1.0,\ 5.0,\ 10.0$ and 20.0. Each panel shows the mean final x-displacement after 100 environmental samples and subsequent movement and $M = 10^4$ agent realisations, interpolated on a 200×200 grid and smoothed with a Gaussian filter. Above each plot is a typical noise landscape, $\eta(x, y)$. At the top right corner of each landscape, the protrusion length in simulations, $l_\mathrm{p} = 5$, is indicated by a black line. In all simulations, $n_\mathrm{p} = l_\mathrm{p} = 5$, and $d = 1$.

In vivo, chemotactic landscapes are rarely perfectly smooth. Local fluctuations arise from pulsatile secretion of chemoattractants (60), variable diffusion barriers in the ECM (61), and competing signals from neighbouring cells (62). Our results suggest that immune cells or amoebae probing environments with very fine-scale heterogeneities (e.g. interstitial tissues with dense ECM pores much smaller than their pseudopod length) will effectively filter out this high-frequency noise and exploit strong front-focused polarity to navigate efficiently. Conversely, in tissues where chemoattractant gradients are distorted over length scales comparable to that of a protrusion, such as in inflamed or tumour-remodelled stroma with tangled fibre networks (63), excessive polarisation may lead cells astray by over-committing to spurious local peaks. Finally, when heterogeneities occur on much larger scales (for example, across organ-scale morphogen gradients (64)), the noise simply shifts the overall baseline and does not create noise at the length-scale of individual protrusions, so that robust polarity once again becomes the optimal strategy. These findings imply that cells may adapt their degree of polarity dynamically by down-regulating bias when local fluctuations match their sensing radius and up-regulating it in very smooth or very coarse environments, in order to maintain reliable chemotaxis across heterogeneous tissues.

In summary, our analysis highlights that optimal protrusive polarity is a context-dependent parameter. Cells must calibrate their angular bias to the reliability of chemoattractant signals. Incorporating mechanisms for feedback-mediated adjustment of κ in response to measured gradient variance would be a natural extension to the model formulated here, allowing for an exploration of how real cells achieve robust chemotaxis across diverse, noisy environments.

3.5 Persistent movement frees cells from local concentration minima and maxima in migration

Cellular persistence refers to the continuous maintenance of a dominant migratory axis across repeated protrusion–retraction cycles and is a well-documented feature of motile cell populations (65). Mechanistically, persistence emerges from interconnected positive-feedback loops involving actin polymerisation and signalling restricted to the leading edge (66, 67). Sustained pseudopod extension at the front of the cell is supported by Rac1-driven activation of the Arp2/3 complex, while PI3K-dependent PIP_3 accumulation further consolidates front-directed polarity. Stabilisation of protrusions and suppression of lateral fluctuations are provided by the maturation of adhesive contacts.

This inherent directional memory may allow cells to bypass misleading local fluctuations in chemoattractant concentration. Furthermore, it may also reduce the energetic demands of frequent environmental sampling in long-distance migration. By maintaining a biased protrusive front, transient adverse gradient cues that obscure global chemical landscapes cannot easily deflect cell trajectories, enabling navigation through small-scale obstacles and the escape of local chemoattractant minima and maxima. *In vivo*, such persistence may contribute to leukocytes squeezing through dense interstitial matrices (68), as well as for developmental cohorts such as cranial neural crest cells that must traverse heterogeneous embryonic tissues in a coherent stream (69).

In this section, we build on this biological foundation to quantify how persistence interacts with our protrusion-based sensing model, increasing energetic efficiency in noise-perturbed chemoattractant profiles. To probe how the frequency of environmental sensing influences chemotactic efficiency under varying noise amplitudes and correlation scales, we extend our agent-based simulations to systematically sweep over the sampling persistence parameter, d, which governs how frequently cells sample their environments with protrusions between successive movement steps. We once again vary the level of spatial heterogeneity in the chemoattractant landscape, quantified by the noise amplitude, σ, and the noise correlation length parameter, ξ. For each parameter combination, we then simulate the ABM for various values of d, which in turn allows us to analyse the evolution of the DTER with respect to the level of persistence in cell movement. At each discrete time point, the cell, again approximated as a point particle, either re-samples the environment with $n_\mathrm{p} = 5$ protrusions, each of length $l_\mathrm{p} = 5$, from a uniform distribution, if d steps have been taken, or moves in its previously chosen direction. Gradient detection logic and parameters are as outlined in the previous section. For each triplet, (σ, ξ, d), we execute $M = 10^4$ independent realisations of the noisy landscape and cell trajectory, each of duration $N = 100$ steps and N/d environmental samples, recording the final net x-displacement, $\mathbf{X}$. By computing the sample mean, $\langle \Delta \mathbf{X} \rangle$, across replicates, we quantify the directional bias of migration under different sensing cadences. Then, quantifying the energy expended by cells in each replicate, according to Equation (10), we compute the average DTER for movement.

As shown in Figure 7, increasing the persistence interval d yields a substantial and monotonic improvement in the DTER across all noise amplitudes, σ, and correlation length parameters, ξ. This effect increases drastically as ξ is increased. The reasons for this are two-fold. In landscapes where noise is correlated over much larger length-scales than the protrusions extended by cells, it is possible for cells that sample local chemical gradients frequently to become trapped in local maxima or minima in chemoattractant concentrations (Figure 7). However, by moving persistently, cells are able to explore a larger proportion of the chemical landscape, and hence, are freed from local extrema in concentration. Furthermore, persistent movement means that cells expend less energy in sampling their environment with protrusions, such that the DTER is further

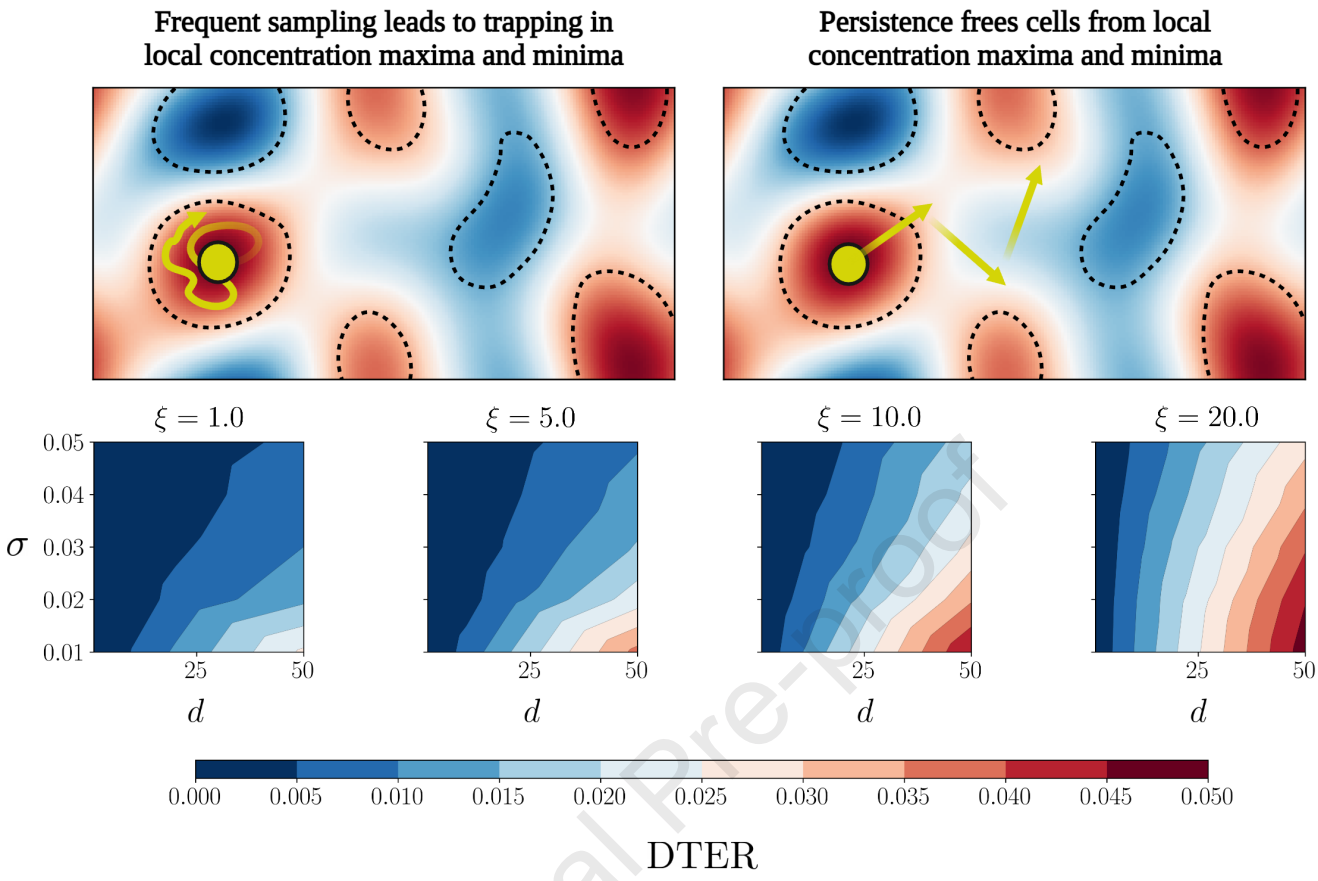

Figure 7: Heatmaps of the DTER, plotted against environmental noise amplitude σ (vertical axis) and sensing interval d (horizontal axis). Panels correspond to noise correlation length parameters ξ = 1.0, 5.0, 10.0, and 20.0. Results are averaged over $M = 10^4$ replicates, and parameters for energy expenditure and gradient detection are fixed at $\alpha_a = \alpha_d = \alpha_m = 1$, $\beta = 10^2$, $k = 10^2/\sqrt{2}$, $\phi = 1$, and $d_{crit} = 0.5$. Panels above the heatmaps illustrate how persistence in movement can free cells from local maxima and minima in chemoattractant concentration. The schematic was produced by Samuel W.S. Johnson in BioRender: https://BioRender.com/d0namxv.

increased.

These findings highlight persistence as a dynamically tunable strategy in chemotaxis. *In vivo*, motile cells may optimise chemotactic navigation by adjusting their sampling–movement cadence in response to local signal noise. Up-regulating persistence in noisy, fluctuating environments conserves energy and allows cells to explore a larger proportion of the global chemoattractant landscape. Consequently, feedback mechanisms that couple measured gradient variance to persistence may be a fundamental biological mechanism for robust, energy-efficient chemotactic migration.

4 DISCUSSION

In this work, we have developed a novel theoretical framework that frames actin-driven protrusive dynamics in eukaryotic chemotaxis as an energetic optimisation problem, wherein cells balance the benefits of chemical gradient detection against the energetic costs of protrusion extension and subsequent movement. The model is qualitatively consistent with several reported trends in protrusive morphology including the bet-hedging-to-speculation transition observed within chick cranial neural crest streams and the biphasic dependence of cell spreading on mechanical substrate properties observed across a range of experimental contexts. This consistency suggests that energetic trade-offs may contribute to shaping the protrusive activity of eukaryotic cells under varying environmental constraints. We do, however, emphasise that these comparisons are qualitative consistency checks rather than formal quantitative validations. In summary, our findings suggest that energy-based trade-offs offer a useful organising lens for interpreting protrusive behaviours, complementing existing mechanistic and signalling-centred

descriptions of chemotaxis.

Several simplifications of the present framework should also be re-stated. The energetic terms in Equation (10) capture the mechanical work associated with cell-body translocation, the elastic deformation of the membrane, and a total dissipative cost proportional to $n_p l_p$ that coarse-grains the metabolically significant dissipative processes underlying protrusion extension, including ATP hydrolysis associated with actin treadmilling, adhesion assembly and turnover, myosin contractility, and receptor-level signal transduction. These contributions are absorbed into a single phenomenological coefficient, together with the one-sided treatment of protrusion energy in which the energy spent in retraction is not recovered. A more detailed description in which these dissipative processes are represented individually, with distinct scalings in n_p and l_p, would be a possible model refinement, though we expect that such a modification would not qualitatively affect our results. On the timescales relevant to protrusion-driven sampling, the assumption that area changes incur a quadratic elastic cost may also overstate the relevant energetic penalty, since cells are permeable and pressure equilibration via fluid flow can relax some of the deformation that a purely elastic treatment would penalise.

For tractability, the model also considers protrusions that are equal in length and width, well-spaced, extended instantaneously, and oriented independently from a prescribed distribution $f(\theta)$. Real pseudopodia are heterogeneous, evolve in time, and often arise through the splitting or stabilisation of existing protrusions rather than *de novo* initiation (22, 29, 45, 70). The framework should, therefore, be interpreted as comparing candidate protrusive phenotypes over a coarse-grained sampling–movement cycle. It does not describe the transient dynamics by which individual protrusions extend, retract, split, or remodel. In this sense, the "optimal" phenotype identified by the model is the combination of protrusion number and length that maximises the prescribed distance-to-energy ratio under fixed environmental conditions, rather than a dynamically attained optimum over the lifetime of an individual protrusion.

A further limitation is that the mechanical energetic terms are derived under a small-deformation, linear-elastic approximation. In particular, the curvature and area-change costs assume that protrusions are sufficiently small relative to the cell body for higher-order geometric corrections and nonlinear membrane/cortex mechanics to be neglected. This approximation is likely to be most appropriate for modest membrane deformations and may break down for large-amplitude protrusions, strong cortical remodelling, or regimes in which membrane tension, adhesion, or cytoskeletal mechanics vary non-linearly with deformation. In such cases, the precise energetic scaling with n_p and l_p may differ from that assumed here, although the broader trade-off between environmental sampling and energetic expenditure would remain a useful organising principle.

As the model formulated here is phenomenological, it is important to verify its predictions with corresponding experiments. One way this could be achieved is through the use of microfluidic devices *in vitro*, which would allow chemoattractant gradients to be perturbed and their effect on cell morphology studied in a controlled manner (71). Substrate stiffness could likewise be tuned using well-established experimental techniques (72), allowing the mechanical environment to be varied systematically. Potential tests of the predictions made here include the systematic variation of chemoattractant gradient steepness *in vitro* to probe the predicted bet-hedging-to-speculation transition within a single cell type, the controlled manipulation of substrate properties across a sufficiently wide stiffness range to expose the predicted biphasic dependence of protrusion number on β within a single cell line, and a study of persistence in noisy chemical landscapes in which the spatial correlation length scale of the imposed noise is varied relative to the characteristic protrusion length. Each of these experiments would isolate a single environmental axis along which the model makes a falsifiable prediction, and together could further refine the predictive power of the model and validate its broader biological applicability.

An important next step involves integrating additional biological realism into the model, such as dynamic protrusion formation and retraction, the consideration of unequal protrusion lengths, and biochemical feedback loops. Allowing protrusions to be initiated by splitting of existing protrusions, rather than independently from a fixed angular distribution, would also bring the framework into closer contact with pseudopod-centred descriptions of chemotaxis (22) and would allow the model to address how the angular distribution $f(\theta)$ itself evolves over a migratory trajectory, which is a known phenomenon in eukaryotic cell chemotaxis (70). Similarly, coupling the substrate parameters β and ϕ to local protease activity would allow the framework to capture the mechano-chemical feedback through which invasive cells sculpt their own microenvironment, as discussed in Section 3.2. Such enhancements would allow for the exploration of transient dynamics in chemotactic sensing and reveal how feedback mechanisms interact with energetic constraints to shape protrusive behaviour over biologically relevant timescales.

In conclusion, our work provides a novel theoretical lens through which to interpret and predict eukaryotic cell morphology in chemotaxis. By elucidating how cells may balance energetic constraints with information acquisition in complex environments, we have contributed to a deeper understanding of cell migration, potentially informing therapeutic strategies targeting pathological migration in processes such as cancer metastasis and immune cell infiltration.

Acknowledgments

S.W.S.J. receives support from the Biotechnology and Biological Sciences Research Council (BBSRC) (grant number BB/T008784/1). R.E.B. is supported by a grant from the Simons Foundation (MP-SIP-00001828). For the purpose of open access, the authors have applied a CC BY public copyright licence to any author-accepted manuscript arising from this submission.

Declaration of interests

The authors declare no conflict of interest.

Authors' contributions

Samuel Johnson: Conceptualisation (lead), data curation (lead); formal analysis (lead); methodology (lead); software (lead); writing–original draft (lead); writing–review and editing (supporting). **Maddy Parsons**: Writing–original draft (supporting); writing–review and editing (lead). **Ruth E. Baker**: Conceptualisation (supporting), supervision (lead); writing–review and editing (lead). **Philip K. Maini:** Conceptualisation (supporting), supervision (lead); writing–review and editing (lead).

Data availability statement

Code used for the generation of figures is not publicly available, but is available from the authors upon reasonable request.

REFERENCES

1. Shellard, A., and R. Mayor, 2016. Chemotaxis during neural crest migration. *Seminars in Cell & Developmental Biology* 55:111–118.

2. Luster, A. D., 2001. Chemotaxis: role in immune response. *Encyclopedia of Life Sciences* 1.

3. Roussos, E. T., J. S. Condeelis, and A. Patsialou, 2011. Chemotaxis in cancer. *Nature Reviews Cancer* 11:573–587.

4. SenGupta, S., C. A. Parent, and J. E. Bear, 2021. The principles of directed cell migration. *Nature Reviews Molecular Cell Biology* 22:529–547.

5. Yeung, T., P. C. Georges, L. A. Flanagan, B. Marg, M. Ortiz, M. Funaki, N. Zahir, W. Ming, V. Weaver, and P. A. Janmey, 2005. Effects of substrate stiffness on cell morphology, cytoskeletal structure, and adhesion. *Cell Motility and the Cytoskeleton* 60:24–34.

6. Lo, C.-M., H.-B. Wang, M. Dembo, and Y.-l. Wang, 2000. Cell movement is guided by the rigidity of the substrate. *Biophysical Journal* 79:144–152.

7. Bosgraaf, L., and P. J. Van Haastert, 2009. Navigation of chemotactic cells by parallel signaling to pseudopod persistence and orientation. *PloS One* 4:e6842.

8. Discher, D. E., P. Janmey, and Y.-l. Wang, 2005. Tissue cells feel and respond to the stiffness of their substrate. *Science* 310:1139–1143.

9. Stroka, K. M., and H. Aranda-Espinoza, 2009. Neutrophils display biphasic relationship between migration and substrate stiffness. *Cell Motility and the Cytoskeleton* 66:328–341.

10. Wang, M., Y. Yang, L. Han, S. Han, N. Liu, F. Xu, and F. Li, 2020. Effect of three-dimensional ECM stiffness on cancer cell migration through regulating cell volume homeostasis. *Biochemical and Biophysical Research Communications* 528:459–465.

11. Tweedy, L., B. Meier, J. Stephan, D. Heinrich, and R. G. Endres, 2013. Distinct cell shapes determine accurate chemotaxis. *Scientific Reports* 3:2606.

12. Andrew, N., and R. H. Insall, 2007. Chemotaxis in shallow gradients is mediated independently of PtdIns 3-kinase by biased choices between random protrusions. *Nature Cell Biology* 9:193–200.

13. Mitchison, T. J., and L. P. Cramer, 1996. Actin-based cell motility and cell locomotion. *Cell* 84:371–379.

14. Small, J. V., T. Stradal, E. Vignal, and K. Rottner, 2002. The lamellipodium: where motility begins. *Trends in Cell Biology* 12:112–120.

15. Wood, W., and P. Martin, 2002. Structures in focus—filopodia. *The International Journal of Biochemistry & Cell Biology* 34:726–730.

16. Petit, V., and J.-P. Thiery, 2000. Focal adhesions: structure and dynamics. *Biology of the Cell* 92:477–494.

17. Pandya, P., J. L. Orgaz, and V. Sanz-Moreno, 2017. Actomyosin contractility and collective migration: may the force be with you. *Current Opinion in Cell Biology* 48:87–96.

18. Swaminathan, V., R. Fischer, and C. M. Waterman, 2016. The FAK–Arp2/3 interaction promotes leading edge advance and haptosensing by coupling nascent adhesions to lamellipodia actin. *Molecular Biology of the Cell* 27:1085–1100.

19. DeWane, G., A. M. Salvi, and K. A. DeMali, 2021. Fueling the cytoskeleton–links between cell metabolism and actin remodeling. *Journal of Cell Science* 134:jcs248385.

20. Wu, Y., M. R. Zanotelli, J. Zhang, and C. A. Reinhart-King, 2021. Matrix-driven changes in metabolism support cytoskeletal activity to promote cell migration. *Biophysical Journal* 120:1705–1717.

21. Zanotelli, M. R., A. Rahman-Zaman, J. A. VanderBurgh, P. V. Taufalele, A. Jain, D. Erickson, F. Bordeleau, and C. A. Reinhart-King, 2019. Energetic costs regulated by cell mechanics and confinement are predictive of migration path during decision-making. *Nature Communications* 10:4185.

22. Insall, R. H., 2010. Understanding eukaryotic chemotaxis: a pseudopod-centred view. *Nature Reviews Molecular Cell Biology* 11:453–458.

23. Rickert, P., O. D. Weiner, F. Wang, H. R. Bourne, and G. Servant, 2000. Leukocytes navigate by compass: roles of PI3Kγ and its lipid products. *Trends in Cell Biology* 10:466–473.

24. Servant, G., O. D. Weiner, P. Herzmark, T. Balla, J. W. Sedat, and H. R. Bourne, 2000. Polarization of chemoattractant receptor signaling during neutrophil chemotaxis. *Science* 287:1037–1040.

25. Xiong, Y., C.-H. Huang, P. A. Iglesias, and P. N. Devreotes, 2010. Cells navigate with a local-excitation, global-inhibition-biased excitable network. *Proceedings of the National Academy of Sciences* 107:17079–17086.

26. Carlsson, A. E., and D. Sept, 2008. Mathematical modeling of cell migration. *Methods in Cell Biology* 84:911–937.

27. Holmes, W. R., and L. Edelstein-Keshet, 2012. A comparison of computational models for eukaryotic cell shape and motility. *PLoS Computational Biology* 8:e1002793.

28. Danuser, G., J. Allard, and A. Mogilner, 2013. Mathematical modeling of eukaryotic cell migration: insights beyond experiments. *Annual Review of Cell and Developmental Biology* 29:501–528.

29. Alonso, A., J. B. Kirkegaard, and R. G. Endres, 2025. Persistent pseudopod splitting is an effective chemotaxis strategy in shallow gradients. *Proceedings of the National Academy of Sciences* 122:e2502368122.

30. Mou, D., and Y. Cao, 2025. Optimal cell shape for accurate chemical gradient sensing in eukaryote chemotaxis. *Physical Review Research* 7:033001.

31. Li, Y., L. Yao, Y. Mori, and S. X. Sun, 2019. On the energy efficiency of cell migration in diverse physical environments. *Proceedings of the National Academy of Sciences* 116:23894–23900.

32. Pontes, B., Y. Ayala, A. C. C. Fonseca, L. F. Romão, R. F. Amaral, L. T. Salgado, F. R. Lima, M. Farina, N. B. Viana, V. Moura-Neto, et al., 2013. Membrane elastic properties and cell function. *PloS One* 8:e67708.

33. Hochmuth, R. M., 2000. Micropipette aspiration of living cells. *Journal of Biomechanics* 33:15–22.

34. Tharp, W. G., R. Yadav, D. Irimia, A. Upadhyaya, A. Samadani, O. Hurtado, S. Liu, S. Munisamy, D. Brainard, M. Mahon, et al., 2006. Neutrophil chemorepulsion in defined interleukin-8 gradients in vitro and in vivo. *Journal of Leukocyte Biology* 79:539–554.

35. Ryan, G. L., D. Holz, S. Yamashiro, D. Taniguchi, N. Watanabe, and D. Vavylonis, 2017. Cell protrusion and retraction driven by fluctuations in actin polymerization: A two-dimensional model. *Cytoskeleton* 74:490–503.

36. Miura, T., 2020. Elastic curves and phase transitions. *Mathematische Annalen* 376:1629–1674.

37. Peskin, C. S., G. M. Odell, and G. F. Oster, 1993. Cellular motions and thermal fluctuations: the Brownian ratchet. *Biophysical Journal* 65:316–324.

38. Mogilner, A., and G. Oster, 1996. Cell motility driven by actin polymerization. *Biophysical Journal* 71:3030–3045.

39. Mogilner, A., and G. Oster, 2003. Force generation by actin polymerization II: the elastic ratchet and tethered filaments. *Biophysical Journal* 84:1591–1605.

40. Prass, M., K. Jacobson, A. Mogilner, and M. Radmacher, 2006. Direct measurement of the lamellipodial protrusive force in a migrating cell. *The Journal of Cell Biology* 174:767–772.

41. Berg, H. C., and E. M. Purcell, 1977. Physics of chemoreception. *Biophysical Journal* 20:193–219.

42. Zaman, M. H., L. M. Trapani, A. L. Sieminski, D. MacKellar, H. Gong, R. D. Kamm, A. Wells, D. A. Lauffenburger, and P. Matsudaira, 2006. Migration of tumor cells in 3D matrices is governed by matrix stiffness along with cell-matrix adhesion and proteolysis. *Proceedings of the National Academy of Sciences* 103:10889–10894.

43. Wolf, K., M. Te Lindert, M. Krause, S. Alexander, J. Te Riet, A. L. Willis, R. M. Hoffman, C. G. Figdor, S. J. Weiss, and P. Friedl, 2013. Physical limits of cell migration: control by ECM space and nuclear deformation and tuning by proteolysis and traction force. *Journal of Cell Biology* 201:1069–1084.

44. McLennan, R., L. J. Schumacher, J. A. Morrison, J. M. Teddy, D. A. Ridenour, A. C. Box, C. L. Semerad, H. Li, W. McDowell, D. Kay, et al., 2015. VEGF signals induce trailblazer cell identity that drives neural crest migration. *Developmental Biology* 407:12–25.

45. Teddy, J. M., and P. M. Kulesa, 2004. In vivo evidence for short-and long-range cell communication in cranial neural crest cells. *Development* 131:6141–6151.

46. Shamloo, A., N. Ma, M.-m. Poo, L. L. Sohn, and S. C. Heilshorn, 2008. Endothelial cell polarization and chemotaxis in a microfluidic device. *Lab on a Chip* 8:1292–1299.

47. McLennan, R., J. M. Teddy, J. C. Kasemeier-Kulesa, M. H. Romine, and P. M. Kulesa, 2010. Vascular endothelial growth factor (VEGF) regulates cranial neural crest migration in vivo. *Developmental Biology* 339:114–125.

48. Bronner, M. E., and N. M. LeDouarin, 2012. Development and evolution of the neural crest: an overview. *Developmental Biology* 366:2–9.

49. Mason, B. N., A. Starchenko, R. M. Williams, L. J. Bonassar, and C. A. Reinhart-King, 2013. Tuning three-dimensional collagen matrix stiffness independently of collagen concentration modulates endothelial cell behavior. *Acta Biomaterialia* 9:4635–4644.

50. Stowers, R. S., S. C. Allen, and L. J. Suggs, 2015. Dynamic phototuning of 3D hydrogel stiffness. *Proceedings of the National Academy of Sciences* 112:1953–1958.

51. Weaver, A. M., 2008. Invadopodia. *Current Biology* 18:R362–R364.

52. Johnson, L. L., R. Dyer, and D. J. Hupe, 1998. Matrix metalloproteinases. *Current Opinion in Chemical Biology* 2:466–471.

53. Page-McCaw, A., A. J. Ewald, and Z. Werb, 2007. Matrix metalloproteinases and the regulation of tissue remodelling. *Nature Reviews Molecular Cell Biology* 8:221–233.

54. Postma, M., L. Bosgraaf, H. M. Loovers, and P. J. Van Haastert, 2004. Chemotaxis: signalling modules join hands at front and tail. *EMBO Reports* 5:35–40.

55. Devreotes, P., and C. Janetopoulos, 2003. Eukaryotic chemotaxis: distinctions between directional sensing and polarization. *Journal of Biological Chemistry* 278:20445–20448.

56. Devreotes, P. N., S. Bhattacharya, M. Edwards, P. A. Iglesias, T. Lampert, and Y. Miao, 2017. Excitable signal transduction networks in directed cell migration. *Annual Review of Cell and Developmental Biology* 33:103–125.

57. Swaney, K. F., C.-H. Huang, and P. N. Devreotes, 2010. Eukaryotic chemotaxis: a network of signaling pathways controls motility, directional sensing, and polarity. *Annual Review of Biophysics* 39:265–289.

58. Huang, C.-H., M. Tang, C. Shi, P. A. Iglesias, and P. N. Devreotes, 2013. An excitable signal integrator couples to an idling cytoskeletal oscillator to drive cell migration. *Nature Cell Biology* 15:1307–1316.

59. Dang, I., R. Gorelik, C. Sousa-Blin, E. Derivery, C. Guérin, J. Linkner, M. Nemethova, J. G. Dumortier, F. A. Giger, T. A. Chipysheva, et al., 2013. Inhibitory signalling to the Arp2/3 complex steers cell migration. *Nature* 503:281–284.

60. Vinet, A. F., T. Fiedler, V. Studer, R. Froquet, A. Dardel, P. Cosson, and J. Pieters, 2014. Initiation of multicellular differentiation in Dictyostelium discoideum is regulated by coronin A. *Molecular Biology of the Cell* 25:688–701.

61. Henke, E., R. Nandigama, and S. Ergün, 2020. Extracellular matrix in the tumor microenvironment and its impact on cancer therapy. *Frontiers in Molecular Biosciences* 6:160.

62. Foxman, E. F., E. J. Kunkel, and E. C. Butcher, 1999. Integrating conflicting chemotactic signals: the role of memory in leukocyte navigation. *The Journal of Cell Biology* 147:577–588.

63. Provenzano, P. P., K. W. Eliceiri, J. M. Campbell, D. R. Inman, J. G. White, and P. J. Keely, 2006. Collagen reorganization at the tumor-stromal interface facilitates local invasion. *BMC Medicine* 4:38.

64. Eldar, A., D. Rosin, B.-Z. Shilo, and N. Barkai, 2003. Self-enhanced ligand degradation underlies robustness of morphogen gradients. *Developmental Cell* 5:635–646.

65. Petrie, R. J., A. D. Doyle, and K. M. Yamada, 2009. Random versus directionally persistent cell migration. *Nature Reviews Molecular Cell Biology* 10:538–549.

66. Costa, C., G. Germena, and E. Hirsch, 2010. Dissection of the interplay between class I PI_3Ks and Rac signaling in phagocytic functions. *The Scientific World Journal* 10:1826–1839.

67. Campa, C. C., E. Ciraolo, A. Ghigo, G. Germena, and E. Hirsch, 2015. Crossroads of PI_3K and Rac pathways. *Small GTPases* 6:71–80.

68. Lämmermann, T., B. L. Bader, S. J. Monkley, T. Worbs, R. Wedlich-Söldner, K. Hirsch, M. Keller, R. Förster, D. R. Critchley, R. Fässler, et al., 2008. Rapid leukocyte migration by integrin-independent flowing and squeezing. *Nature* 453:51–55.

69. Kulesa, P. M., C. M. Bailey, J. C. Kasemeier-Kulesa, and R. McLennan, 2010. Cranial neural crest migration: new rules for an old road. *Developmental Biology* 344:543–554.

70. Genuth, M. A., C. D. Allen, T. Mikawa, and O. D. Weiner, 2018. Chick cranial neural crest cells use progressive polarity refinement, not contact inhibition of locomotion, to guide their migration. *Developmental Biology* 444:S252–S261.

71. Kim, S., H. J. Kim, and N. L. Jeon, 2010. Biological applications of microfluidic gradient devices. *Integrative Biology* 2:584–603.

72. Tse, J. R., and A. J. Engler, 2010. Preparation of hydrogel substrates with tunable mechanical properties. *Current Protocols in Cell Biology* 47:10–16.

APPENDIX A: MODEL PARAMETER SWEEP

Variation in the parameters of the model for $f(\theta) = \mathrm{U}[0, \pi]$ and

$$g(\beta, \phi) = \frac{\phi\beta}{k} \exp\left(-\left(\frac{\beta}{k}\right)^2\right), \tag{38}$$

shows that the optimal protrusive phenotype varies with both the energetic parameters and the environmental parameters of the model (Figures 8–10). For a fixed value of d_{crit}, varying the energetic parameters changes the absolute value of $n_{\mathrm{p}}^{\mathrm{opt}}$. In general, $n_{\mathrm{p}}^{\mathrm{opt}}$ increases when cells become more motile through an increase in ϕ, or when the energetic cost of movement, α_{m}, is increased. Conversely, increasing the energetic cost associated with membrane deformation, α_{a}, or protrusion assembly, α_{d}, decreases $n_{\mathrm{p}}^{\mathrm{opt}}$. These trends reflect the trade-off between the energetic costs of protrusive sampling and the energetic consequences of moving in a suboptimal direction. When movement is costly relative to protrusion formation, it is favourable to sample the environment more extensively prior to movement, thereby increasing the probability that movement occurs in the direction of the chemical gradient. Conversely, when protrusion formation is costly relative to movement, the optimal strategy is to sample fewer directions and tolerate a greater risk of suboptimal movement.

Across the parameter ranges explored, we find that the qualitative effect of d_{crit} is robust. Increasing d_{crit}, which corresponds to increasing the characteristic length scale of the imposed chemical gradient, results in a monotonic decrease in $n_{\mathrm{p}}^{\mathrm{opt}}$, up to plateaux arising from the integer-valued nature of $n_{\mathrm{p}}^{\mathrm{opt}}$. Thus, Figures 8–10 together show that the bet-hedging-to-speculation transition discussed in Section 3.1 exists across a broad space of model parameters.

This trend is accompanied by a corresponding change in $l_{\mathrm{p}}^{\mathrm{opt}}$. In general, across the parameter values considered, $l_{\mathrm{p}}^{\mathrm{opt}}$ remains close to the smallest integer value that exceeds the threshold distance for gradient detection, d_{crit}. Thus, as gradients become harder to detect, the model favours protrusions that are minimally long enough to resolve the gradient, rather than substantially longer protrusions that would incur additional energetic cost. The decrease in $n_{\mathrm{p}}^{\mathrm{opt}}$ with increasing d_{crit}, therefore, arises as shallow chemical gradients drive cells to extend longer protrusions, increasing the energetic penalty associated with each additional protrusion.

We also find that the biphasic dependence of optimal protrusive activity on the effective substrate resistance, β, is robust across parameter space. For small values of β, cells gain little directed displacement from protrusive sampling, such that the energetic return on extending many protrusions is low and $n_{\mathrm{p}}^{\mathrm{opt}}$ remains small. At intermediate values of β, substrate conditions permit greater movement following successful gradient detection, and the optimal strategy shifts towards larger $n_{\mathrm{p}}^{\mathrm{opt}}$ in order to optimise the direction of movement. For sufficiently large values of β, movement is again suppressed, and the benefit of additional protrusive sampling decreases, causing $n_{\mathrm{p}}^{\mathrm{opt}}$ to fall. The resulting biphasic relationship persists across the explored energetic parameter ranges, indicating that the substrate resistance prediction in the main text is not restricted to the baseline parameter set.

We note that this biphasic dependence on β reflects the assumed substrate-dependent motility function $g(\beta, \phi)$, which encodes reduced movement in both very low- and very high-resistance environments. The parameter sweep therefore shows that, once such a biphasic motility–resistance relationship is imposed, the predicted biphasic response in $n_{\mathrm{p}}^{\mathrm{opt}}$ is robust to a variation in the remaining model parameters.

APPENDIX B: MODEL ASSUMPTIONS AND SCOPE

We highlight and explain the primary modelling assumptions used in formulating the DTER model and hence, in deriving Equation (20).

Two-dimensional cell geometry We represent the cell as a disk of radius l_0, with its membrane represented by a closed one-dimensional elastic loop. This reduction is used so that protrusion number, protrusion length, angular orientation, and membrane deformation can all be defined within the same planar geometry. Each protrusion is characterised by a length, l_{p}, and an angle, θ, and successful gradient sensing depends on the projection $l_{\mathrm{p}} \cos\theta$ in the direction of the imposed chemical gradient. The two-dimensional geometry, therefore, underpins the calculation of membrane deformation energy and the gradient sensing calculation through the order statistics of the sampled protrusion orientations. The main limitation of this convention is that the model does not resolve the full three-dimensional cell surface. It neglects out-of-plane protrusions, changes in cell volume, and spatial variation in membrane or cortical mechanics over the cell surface.

Energy budget. The energy budget distinguishes the costs of protrusion formation from the cost of subsequent cell-body translocation. Before non-dimensionalising Equation (20) by fixing $\alpha_{\mathrm{b}} = 1$, the protrusion formation cost contains a bending

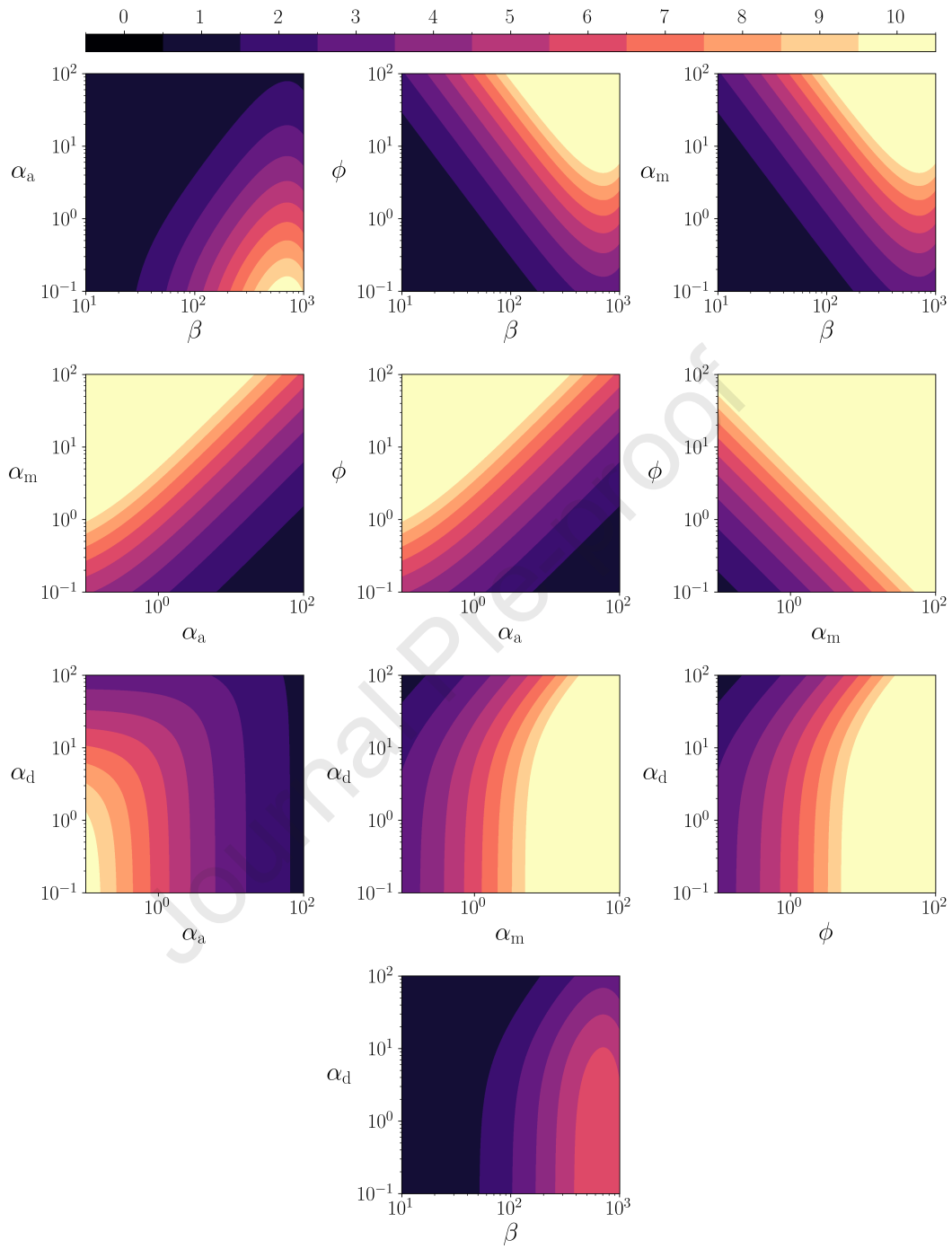

Figure 8: n_p^{opt} as a function of various parameter pairings for the base case of $\alpha_a = \alpha_d = \alpha_m = \phi = 1$, $\beta = 5 \times 10^2$, and $k = 5\sqrt{2} \times 10^2$, with $d_{crit} = 0.5$. Heatmaps show n_p^{opt} when two of these model parameters are varied. In general, increasing the cost of membrane deformation or protrusion assembly decreases n_p^{opt}, whereas an increase in the cost of movement, or the distance moved between the extension of protrusions, increases n_p^{opt}. At all parameter combinations, l_p remains at the lowest or next-lowest integer value above the threshold distance for detection ($d_{crit} = 0.5$, $l_p = 1$ or 2). Please note that optimisation occurs for $n_p \in \{1, ..., 10\}$ and that globally optimum values do not lie in this range across all parameter combinations shown.

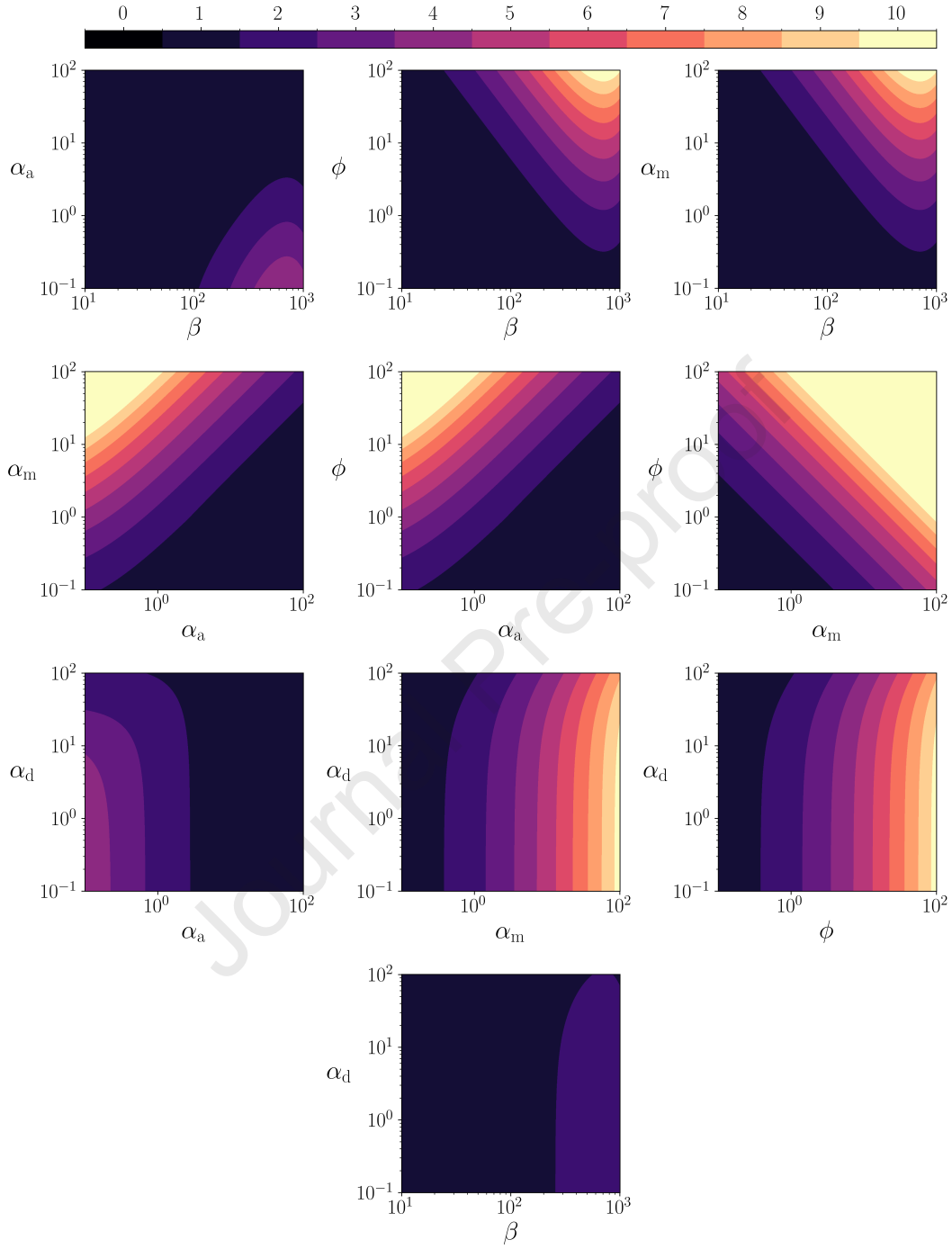

Figure 9: n_p^{opt} as a function of various parameter pairings for the base case of $\alpha_a = \alpha_d = \alpha_m = \phi = 1$, $\beta = 5 \times 10^2$, and $k = 5\sqrt{2} \times 10^2$, with $d_{crit} = 3.5$. Heatmaps show n_p^{opt} when two of these model parameters are varied. In general, increasing the cost of membrane deformation or protrusion assembly decreases n_p^{opt}, whereas an increase in the cost of movement, or the distance moved between the extension of protrusions, increases n_p^{opt}. Across the majority of the parameter space considered, l_p remains at the lowest or next-lowest integer value above the threshold distance for detection ($d_{crit} = 3.5, l_p = 4$ or 5). Please note that optimisation occurs for $n_p \in \{1, ..., 10\}$ and that globally optimum values do not lie in this range across all parameter combinations shown.

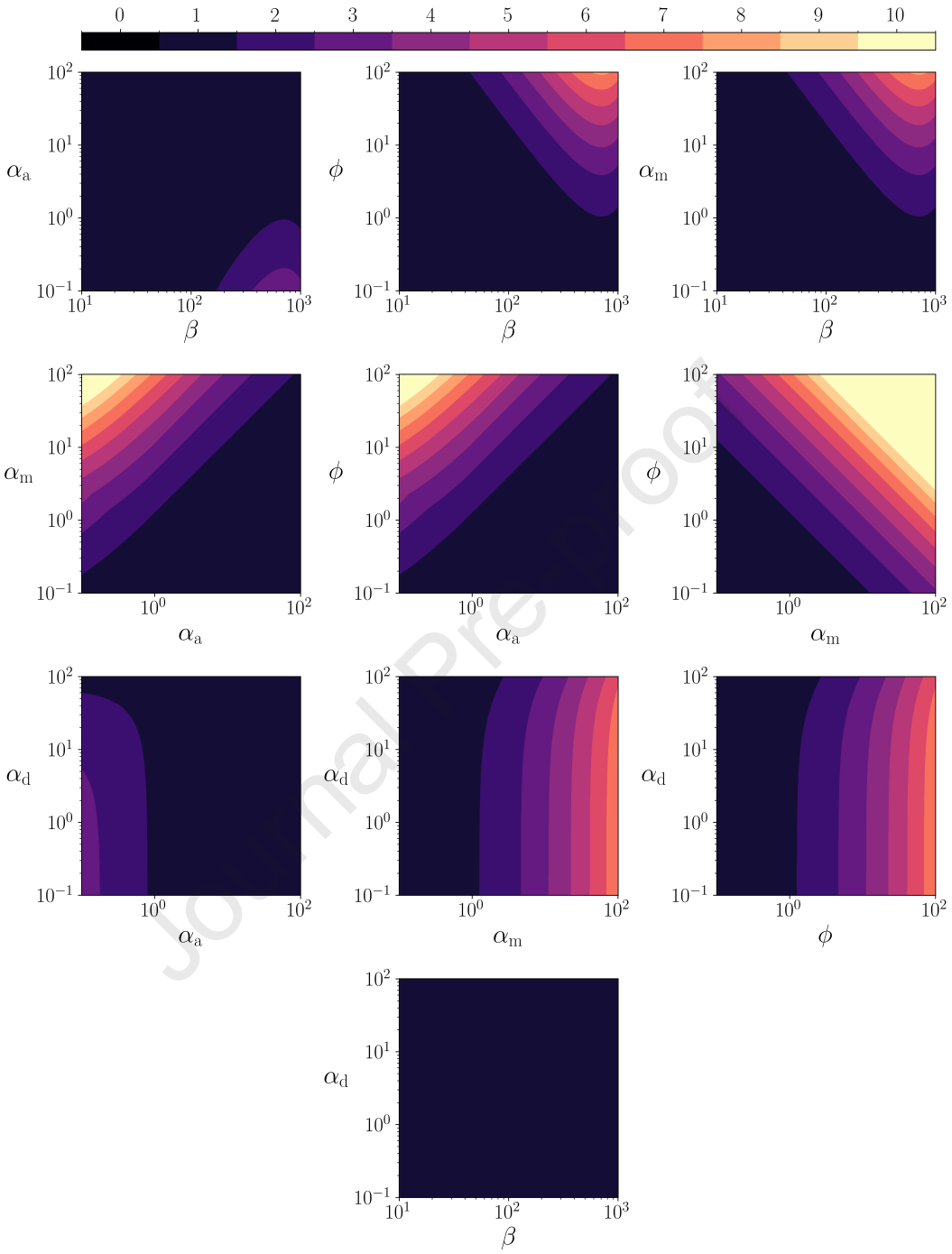

Figure 10: n_p^{opt} as a function of various parameter pairings for the base case of $\alpha_a = \alpha_d = \alpha_m = \phi = 1$, $\beta = 5 \times 10^2$, and $k = 5\sqrt{2} \times 10^2$, with $d_{crit} = 6.5$. Heatmaps show n_p^{opt} when two of these model parameters are varied. In general, increasing the cost of membrane deformation or protrusion assembly decreases n_p^{opt}, whereas an increase in the cost of movement, or the distance moved between the extension of protrusions, increases n_p^{opt}. Across the majority of the parameter space considered, l_p remains at the second- or third-lowest integer value above the threshold distance for detection ($d_{crit} = 6.5, l_p = 8$ or 9). Please note that optimisation occurs for $n_p \in \{1, ..., 10\}$ and that globally optimum values do not lie in this range across all parameter combinations shown.

term, $\alpha_b n_p l_p^2$, an area-elastic term, $\alpha_a n_p^2 l_p^2$, and a dissipative term, $\alpha_d n_p l_p$. The first two terms represent reversible mechanical deformation of the membrane and cortex, whereas the third represents irreversible processes associated with protrusive sampling, including actin turnover, adhesion turnover, contractility, and receptor-level sensing. The remaining term represents the effective work required to translocate the cell body after sampling. In Equation (10) this is written as $\alpha_m \beta d$, where β is the effective mechanical resistance of the surrounding medium and d is the distance moved upon environmental sampling. In the final DTER expression (Equation (19)), this distance is rescaled by the substrate-dependent motility factor $g(\beta, \phi)$, giving the movement cost $\alpha_m \beta g(\beta, \phi) d$.

Quasi-static protrusive sampling. A protrusive phenotype in the model is specified entirely by n_p and l_p, and its energetic cost is evaluated without accounting for the finite time windows of protrusion growth and retraction. Thus, the model compares sampling strategies at a single point in time (the point at which protrusions are fully extended). The optimum obtained from Equation (20) should, therefore, be interpreted as an energetic preference over a protrusive sampling cycle. It is not a prediction of the order in which protrusions appear, how long they persist, or how they are retracted.

Protrusion shape and spacing. Each protrusion is treated as a Gaussian deformation of a fixed width and a length l_p. For protrusions of this form, the curvature contribution scales as l_p^2; assuming that protrusions are well-spaced then gives the additive bending cost $E_b = \alpha_b n_p l_p^2$. The area term uses the corresponding fixed-width scaling and gives $E_a = \alpha_a n_p^2 l_p^2$. For analytic tractability, these formulae assume that protrusions do not overlap on the membrane of the cell, as this would require us to modify the expression for membrane bending energy, and in doing so, consider every possible configuration of n_p and l_p in which protrusions can overlap.

Angular sampling. The protrusion angles are sampled independently from a prescribed distribution, $f(\theta)$. This assumption is what allows the expected drift to be written in terms of the minimum sampled angle and its order statistic density. It also facilitates the comparison of unbiased protrusion generation with front-biased protrusion generation by changing $f(\theta)$, without changing the rest of the model. What is omitted from this formulation are correlations between protrusion orientations in time, which have been documented in the experimental literature (70). The model also does not include pseudopod splitting (29). The addition of these mechanisms would represent a considerable development of the model considered here, and would drastically increase the space of protrusive strategies to analyse.

Gradient detection. In the single-protrusion sensing model, a gradient is detected only if a protrusion extends far enough in the gradient direction. This condition is encoded by d_{crit}, or equivalently by the angle $\theta_{crit} = \cos^{-1}(d_{crit}/l_p)$ when $l_p \geq d_{crit}$. Larger values of d_{crit} correspond to gradients that are harder to resolve, or to weaker effective sensitivity of the cell. This threshold formulation avoids having to model receptor binding, ligand noise, amplification, and adaptation explicitly. It reduces these sensing processes to the question of whether a protrusion spans a sufficient concentration difference. In Section 3.3, a similar representation of the chemical gradient is used in the formulation of the integrated sensing mechanism, where the relevant distance is instead the separation in the gradient direction between the tips of two protrusions extended along the cell membrane.

Substrate-dependent motility. The function $g(\beta, \phi)$ modifies the distance moved after protrusive sampling. In the results sections, it is chosen to represent a biphasic relationship between motility and substrate stiffness in which very soft substrates limit traction, while very stiff or dense substrates impede movement. The parameter ϕ represents permissive features of the substrate, such as alignment or architecture, that increase movement for a given value of β. Thus, the model does not derive the biphasic motility–stiffness curve. It takes such a relationship as an input and asks how the optimal n_p and l_p change once movement through the environment is altered in this way.